Filling the gap of wind observations inside tropical cyclones

Article

Tridon, F. ORCID: https://orcid.org/0000-0002-0436-283X, Battaglia, A. ORCID: https://orcid.org/0000-0001-9243-3484, Rizik, A., Scarsi, F. E. and Illingworth, A. ORCID: https://orcid.org/0000-0002-5774-8410 (2023) Filling the gap of wind observations inside tropical cyclones. Earth and Space Science, 10 (11). e2023EA003099. ISSN 2333-5084 doi: 10.1029/2023ea003099 Available at https://centaur.reading.ac.uk/114685/

To link to this article DOI: http://dx.doi.org/10.1029/2023ea003099

Publisher: American Geophysical Union (AGU)

Earth and Space Science

RESEARCH ARTICLE

10.1029/2023EA003099

Filling the Gap of Wind Observations Inside Tropical Cyclones

F. Tridon[1], **A. Battaglia**[1,2,3], **A. Rizik**[1], **F. E. Scarsi**[1], **and A. Illingworth**[4]

[1]Dipartimento di Ingegneria dell'Ambiente, del Territorio, Politecnico di Torino, Turin, Italy, [2]Department of Physics and Astronomy, University of Leicester, Leicester, UK, [3]National Center for Earth Observation, Leicester, UK, [4]Department of Meteorology, University of Reading, Reading, UK

Key Points:

- Attenuation makes a spaceborne 94 GHz radar blind for only 5% of the cloudy/precipitating part of tropical cyclones (TCs)
- Thanks to its scanning capability, WIVERN would provide about 50 times more observations in TCs than the CloudSat sampling of clouds
- WIVERN wind uncertainty is dominated by pulse-pair estimator noise (3 m/s at 1 km horizontal resolution and reflectivity exceeding −15 dBZ)

Correspondence to:

F. Tridon,
frederic.tridon@polito.it

Citation:

Tridon, F., Battaglia, A., Rizik, A., Scarsi, F. E., & Illingworth, A. (2023). Filling the gap of wind observations inside tropical cyclones. *Earth and Space Science*, *10*, e2023EA003099. https://doi.org/10.1029/2023EA003099

Received 13 JUN 2023
Accepted 26 SEP 2023

Author Contributions:

Conceptualization: F. Tridon, A. Battaglia, A. Illingworth
Data curation: F. Tridon, A. Rizik, F. E. Scarsi
Formal analysis: F. Tridon
Funding acquisition: A. Battaglia, A. Illingworth
Methodology: F. Tridon, A. Battaglia
Project Administration: A. Battaglia, A. Illingworth
Software: F. Tridon, A. Battaglia, A. Rizik
Supervision: A. Battaglia
Validation: F. Tridon, A. Battaglia
Visualization: F. E. Scarsi
Writing – original draft: F. Tridon, A. Battaglia
Writing – review & editing: A. Rizik, A. Illingworth

Abstract The WIVERN (WInd VElocity Radar Nephoscope) mission, currently under the Phase-0 of the ESA Earth Explorer program, promises to provide new insight in the coupling between winds and microphysics by globally observing, for the first time, vertical profiles of horizontal winds in cloudy areas. The objective of this work is to explore the potential of the WIVERN conically scanning Doppler 94 GHz radar for filling the wind observation gap inside tropical cyclones (TCs). To this aim, realistic WIVERN notional observations of TCs are produced by combining the CloudSat 94 GHz radar reflectivity observations from 2007 to 2009 with ECMWF co-located winds. Despite the short wavelength of the radar (3 mm), which causes strong attenuation in presence of large amount of liquid hydrometeors, the system can profile most of the TCs, particularly the cloudy areas above the freezing level and the precipitating stratiform regions. The statistical analysis of the results shows that, (a) because of its lower sensitivity, a nadir pointing WIVERN would detect 75% of the clouds observed by CloudSat (45% of winds with 3 m s^{-1} accuracy, in comparison to CloudSat sampling of clouds), (b) but thanks to its scanning capability, WIVERN would actually provide 53 times more observations of clouds than CloudSat in TCs (30 times more observations of horizontal winds), (c) this corresponds to about 350 (200) million observations of clouds (accurate winds) every year. Such observations could be used to shed light on the physical processes underpinning the evolution of TCs and in data assimilation in order to improve numerical weather prediction.

Plain Language Summary Despite their huge impact on tropical weather, tropical cyclones are still not fully understood with uncertainties in the predictions of their evolution and trajectory. In order to provide more detailed observations of tropical cyclones, a ground-breaking spaceborne observing system hosting a conically scanning Doppler high frequency radar that could provide information both on in-cloud winds and cloud mass contents is proposed. Despite the fact that the observations from such radar are strongly attenuated in presence of heavy rain, the system can sample most of the tropical cyclones, particularly the cloudy areas above the freezing level and the precipitating stratiform regions. Our notional study, based on the climatology of tropical cyclones collected during 3 years by a spaceborne nadir pointing non-Doppler radar, demonstrates that the newly proposed satellite would provide hundred millions observations of clouds and accurate winds in tropical cyclones every year. Such observations could be used to improve our understanding of the processes underpinning the evolution of tropical cyclones and hence, their forecast.

1. Introduction

Tropical cyclones (TCs) are the most iconic weather system. They play a paramount role in the Earth's radiation budget and in the water cycle by transporting heat and moisture from the tropics to the mid-latitudes (Emanuel, 2001; Scoccimarro et al., 2011) and by releasing huge quantities of latent heat (Emanuel, 2003). But most importantly, they are among the most devastating of natural disasters causing widespread destruction due to strong wind and excessive amounts of rainfall when making landfall (Klotzbach et al., 2018).

There is still no widespread consensus on the understanding and prediction of the genesis of TCs (Emanuel, 2003). Several studies have found that environmental vertical wind shear (usually defined between 200 and 850 hPa) is the main driver for the formation, intensification, and dissipation of TCs because of its capability of causing kinematic and thermodynamic asymmetries (Schenkel et al., 2020; Thatcher & Pu, 2011; Wadler et al., 2022) but intertwined complex multiscale processes generally govern TC intensity change (Judt & Chen, 2016). The understanding of the dynamical and thermodynamical structure, of the cloud microphysics and its evolution during TC's life cycle is still a matter of active research and is crucial to improve forecasts (R. Rogers et al., 2013).

Another challenge with TCs is to predict their frequency and intensity response in a changing climate. This has been the subject of considerable investigation, often with conflicting results (Emanuel, 2021; Knutson et al., 2010). One of the factors explaining such inconsistencies is the differences in model physics (Walsh et al., 2016). Indeed, even with high resolution forecast models, biases in the physics were found to be responsible for a degradation of the forecasts of strong TCs when assimilating observations (Tong et al., 2018). To be confident in the predictions about the frequency of TCs in a future climate, it is important that the models are physically based and not empirically tuned.

Airborne radar observations have been used to understand mesoscale and convective-scale processes (e.g., convective bursts, downdrafts near the warm core, vortex Rossby waves, eyewall asymmetries) associated with the cyclone intensity change (R. F. Rogers et al., 2016; Guimond et al., 2020; Didlake et al., 2017; Wadler et al., 2018). Many observations and numerical experiments suggest the positive impact of assimilating wind observations, and in particular radar Doppler velocity observations, on forecasting TC track, structure, intensity and rainfall prediction (J. E. George & Gray, 1976; Bucci et al., 2021; Feng et al., 2023, and references therein). For example, Tong et al. (2018) highlight the benefit of assimilating aircraft reconnaissance observations in improving TCs track and intensity forecasts. However, many TCs are too far out over the ocean to be reached with current manned aircraft and reconnaissance flight missions are primarily conducted for potentially landfalling storms, or they require long-duration unmanned aircraft such as the Global Hawk (Sippel et al., 2014). Progress is still hampered by the lack of high-resolution observations of the spatio-temporal evolution of the TC vertical structure of winds and clouds, especially over the oceans.

Satellite observations of winds can fill this gap. For example, recent studies have tested the impact of assimilating atmospheric motion vectors (AMVs) (Wu et al., 2014; C. Velden et al., 2017) or surface winds derived from ocean surface layer (Cui et al., 2019; Leidner et al., 2018). One limitation of such observations is that they are representative of a specific height, which can even be uncertain in the case of AMVs (C. S. Velden & Bedka, 2009; Cordoba et al., 2017). In 2018, the European Space Agency (ESA) launched the first spaceborne Doppler lidar (Aeolus) (Stoffelen et al., 2005) for measuring line-of-sight winds over an atmospheric column. This mission has been a fantastic success demonstrated by the operational follow-on mission called Aeolus-2 which should be launched within a decade (Wernham et al., 2021). It was shown that the assimilation of Aeolus observations generally improved forecasts of several numerical weather prediction models (NWP) (G. George et al., 2021; Rennie et al., 2021; Laroche & St-James, 2022). This includes positive impact in the forecast of TC intensity and size (Marinescu et al., 2022), despite Aeolus measurements being made in clear air and thin clouds, and mostly coming from upper troposphere and lower stratosphere. However, it is well known that the tropospheric winds have a crucial role in steering TC tracks (J. E. George & Gray, 1976) and that assimilation of inner core—where most of the rain bands are present—winds is particularly useful for improving forecasts (Feng et al., 2023; Tong et al., 2018). Thus, because of the lack of penetration capability of lidar inside cloudy and rainy systems, this will remain an observation gap even in the Aeolus2 era.

The WIVERN (WInd VElocity Radar Nephoscope) mission (www.wivern.polito.it Illingworth et al., 2018; Battaglia et al., 2022), currently in Phase-0 within the ESA Earth Explorer program, promises to complement the Aeolus measurements, with a concept similar to the Radar Wind Sounder proposed by Moore et al. (1996) or the DYCECT mission proposed by Lemaître and Viltard (2013). For the first time, it would provide global observations of vertical profiles of winds in cloudy and rainy areas thanks to a conically scanning W-band (94 GHz) radar with polarization diversity capability. The objective of the mission is to extend the lead time of predictions of high-impact weather, including TCs and mid-latitude windstorms, and to improve short and medium-range weather forecasts by feeding, at a global scale, the Doppler measurements together with profiles of radar reflectivity and km-scale 94 GHz brightness temperatures into NWP models. It will provide global coverage about once a day with 500 m vertical and 10 km resolution with an accuracy of 2 m s^{-1}. Such data can be assimilated into NWP models to improve the forecasting of the future track and intensity of TCs.

It is expected that the WIVERN 94 GHz radar will suffer from attenuation and multiple scattering effects in the presence of heavy rain and large amounts of ice contents (Battaglia et al., 2010; Matrosov et al., 2008; Protat et al., 2019). In addition, the reduced WIVERN radar sensitivity compared to W-band non-scanning radars like the nadir-looking CloudSat and EarthCARE cloud profiling radars (Illingworth et al., 2015; Tanelli et al., 2008) will lower its cloud detection capabilities. The scope of this paper is to evaluate the importance of these detrimental effects and to assess the potential of the WIVERN mission to "see" inside TCs and provide

Table 1
Specifics Currently Envisaged for the Polarization Diversity Doppler Radar of the WIVERN Mission

Spacecraft height, H_{sat}	500 km
Spacecraft velocity, v_{sat}	7,600 m s^{-1}
Incidence angle, θ_i	41.6°
Radar frequency	94.05 GHz
Pulse length τ	3.3 μs
Antenna beamwidth, θ_{3dB}	0.071°
Antenna angular velocity, Ω_a	12 rpm
Footprint speed	500 km s^{-1}
Transmit polarization	H or V
Time separation between H and V pulses, T_{HV}	20 μs
Single pulse sensitivity	−15 dBZ
H-V Pair Repetition Frequency	4 kHz
Number of H-V Pairs per 1 km integration length	8

simultaneous information about horizontal winds and cloud microphysics. Following Battaglia et al. (2018), this work exploits the multi-year CloudSat 94 GHz radar observations of TCs (Tourville et al., 2015) in combination with ECMWF reanalysis in order to simulate WIVERN-like W-band Doppler observations.

Section 2 describes the methodology for simulating WIVERN observations starting from the CloudSat Tropical Cyclone Product; a statistical analysis on the expected performances from the radar is reported in Section 3, including the budget of wind measurements error in Section 3.4. Conclusions are drawn in Section 4.

2. Simulating WIVERN Measurements From Existing Observations

The specifics of the WIVERN radar are listed in Table 1. It is a 94 GHz conically scanning radar with a large antenna (about 3 m) and an off-zenith viewing angle of about 42°, chosen to sample a significant component of horizontal winds, and as a compromise between maximal coverage and minimal range (the latter allowing to maximize the signal-to-noise ratio). As the antenna spins around at 12 rpm, it covers an 800-km wide swath and will make multiple observations of winds in every tropical cyclone about once a day (Illingworth et al., 2018). Thanks to its fast conical rotation speed (footprint moving at about 500 km s^{-1}), WIVERN will sample weather features with a much better sampling rate than a non-scanning radar (e.g., 66 times larger than CloudSat radar whose footprint moves at 7.6 km s^{-1}). Assuming that the typical radius of TCs is 1000 km, it is possible to show that in a pure geometrical sense, the WIVERN sampling of TCs will be about 70 times better than CloudSat (see Appendix A). The objective of this work is to assess the effect of the WIVERN radar sensitivity on this number.

The WIVERN radar will collect 2D curtains of reflectivity in the horizontal (H) and vertical polarizations (V), and Doppler velocities (Fabry, 2015), with 500 m vertical resolution inside the hurricane from all possible directions. Like for Aeolus, WIVERN line-of-sight (LoS) winds are foreseen to be assimilated in NWP models, but with the clear advantage of measuring winds in every direction (while Aeolus measured only zonal winds). It will also be possible to reconstruct horizontal wind vectors within a ~200 km band around mid-scan on both sides of the satellite path, where two nearly orthogonal LoS observations are available (see the WIVERN scanning pattern shown in Figure 1. However, the number of samples of such product will be strongly reduced and it will be more effective to directly assimilate LoS winds.

2.1. Simulation Inputs: CloudSat Reflectivity Curtains and ECMWF Winds

In order to simulate WIVERN measurements, the best proxies are provided by the CloudSat 94 GHz nadir-looking Cloud Profiling Radar (CPR) (Tanelli et al., 2009), together with winds from the ECMWF model. CloudSat has successfully collected data for more than 15 years and provided global observations of the cloud vertical structure of TCs with high resolution. The ECMWF model winds are on the average unbiased (0.2 m s^{-1}) but statistical comparisons with Aeolus observations show that individual winds have a random error standard deviation of about 3 m s^{-1} (Rennie et al., 2021). A major limitation of the ECMWF winds is their coarse resolution which smooths out the variations. For example, Houchi et al. (2010) showed that the model can underestimate the wind shear by 10 times in comparison to high resolution radiosonde wind profiles. Hence, it should be noted that the ECWMF winds may not be fully representative of the actual wind shears.

Tourville et al. (2015) combined these two datasets leading to a collection of more than 10 million TC profiles of reflectivity and horizontal winds. Following the idea of Battaglia et al. (2018), WIVERN slant-looking reflectivity observations can be reconstructed from CloudSat nadir-looking radar observations of TCs, and WIVERN Doppler velocities can be simulated from ECMWF winds.

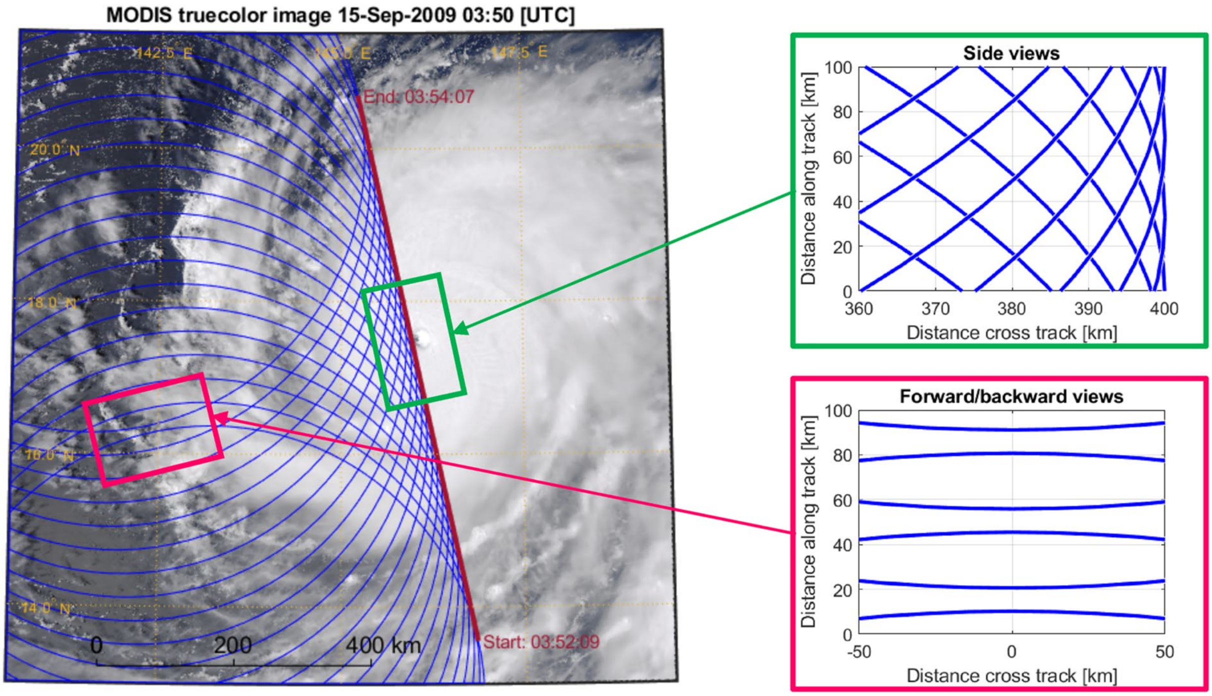

Figure 1. Visible image from the AQUA MODIS satellite of the Choi-Wan typhoon on 15 September 2009 between 03:51:38 and 03:54:37 with the CloudSat trajectory (red line) and the simulated scanning pattern of the conically scanning WIVERN radar as if it were observing the typhoon eye in side-view (blue line, 23 rotations, 115 s). The insets on the right show details of the region swept by the 3-dB footprints close to side views and to forward/backward views.

2.2. Simulation Procedure

The details about the simulation methodology are given in Appendix B. In this section, we describe only the new features of the simulator which have been added in this study in comparison to Battaglia et al. (2018). Here, the non-uniform-beam-filling (NUBF) and wind shear (WS) effects are largely discussed because some of the new features allow to take them into account in a better way. However, these effects have a minor impact on the Doppler velocity precision, and the final accuracy of WIVERN measurements will be mainly driven by the Doppler estimation (see discussion later in Section 3.4).

1. Instead of discarding entire CloudSat profiles where strong attenuation makes the ocean surface invisible and hence, prevents the application of the surface reference technique (Meneghini et al., 2000), an iterative attenuation correction (Hitschfeld & Bordan, 1954) is applied down to the level where a 10 dB cumulative attenuation is reached. This preserves the original structure of the 2D reflectivity field and ensures realistic reflectivity gradients necessary for the correction of NUBF and WS effects.
2. The procedure described in the first item allows the inclusion of all surfaces and not only the ocean surfaces where a CloudSat path integrated estimate is possible via the surface reference technique (Meneghini et al., 2000). As a result, the entire CloudSat orbits can now be mapped into WIVERN observations.
3. In addition to the simulation of WIVERN observations in the forward direction, the option to simulate WIVERN Doppler velocity in the side direction has been added. This allows to simulate the two extreme configurations where the satellite velocity has a maximum (forward) and minimum (side) contribution to NUBF error. In the forward view, the slant geometry of WIVERN is reconstructed from several successive CloudSat profiles, and the resulting vertical reflectivity gradients are used for NUBF and WS corrections. In the side view, the reflectivity is assumed to be horizontally homogeneous along the pointing direction, and the variability of the CloudSat reflectivity field allows to compute realistic horizontal gradients, which are the relevant gradients for the correction of NUBF error in this pointing direction. Another advantage of simulating WIVERN along the forward and side directions is that it provides more representative statistics of winds, with the forward view dominated by meridional winds and the side view dominated by zonal winds.

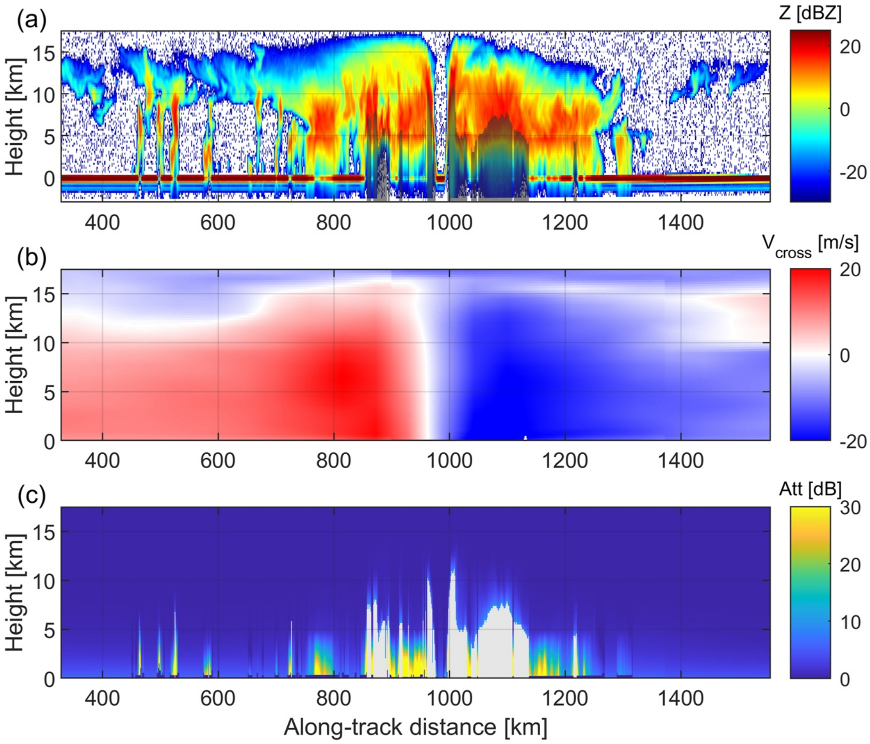

Figure 2. (a) CloudSat reflectivity curtain from the segment of granule 17,996 corresponding to the overpass of the typhoon Choi-Wan on the 15 Sep 2009, (b) corresponding ECMWF wind in the direction across the CloudSat track (at 41° incidence angle), (c) path integrated attenuation retrieved by 2C-RAIN-PROFILE product or with the Hitschfeld and Bordan (1954) technique when the surface is not visible.

2.3. Example of the Typhoon Choi-Wan

The methodology is demonstrated in a case study: the typhoon Choi-Wan, a category 5-equivalent super typhoon that developed over the Western Pacific in September 2009. Despite its intensity, no casualties were reported because its trajectory remained far from major inhabited land, only passing close to the Northern Mariana Islands. On 11 September 2009, a tropical depression formed 1,100 km to the east of Guam and rapidly intensified into a TC. The intensification persisted through the following days until September 15, when Choi-Wan attained its peak intensity, with sustained winds peaking at 260 km hr^{-1}. The typhoon remained very powerful until September 17 and weakened rapidly after September 19 to the East of Japan. Its high impact on ocean temperature, salinity and CO2 partial pressure was studied in Bond et al. (2011). On September 15, the A-train satellites made an overpass just north of the eye at the center of the storm, as shown by MODIS satellite visible observations (Figure 1) and the CloudSat Cloud Profiling Radar reflectivity curtain (Figure 2a).

Figure 2 shows the CloudSat radar reflectivity observations (Figure 2a), the cross-track ECMWF winds (Figure 2b) and the cumulative two-way attenuation (Figure 2c) derived from the CloudSat 2C-RAIN-PROFILE product (Haynes et al., 2009). The whole curtain is over the Pacific ocean as highlighted by the strong surface return. The radar reflectivity captures the vertical cross-section of the storm with its cloud structure. Most distinctive is the eye, which is completely clear down to sea level with thick clouds on either side of the eye towering in the inner eyewall region above 15 km. The transition between frozen and liquid precipitation is outlined by the radar bright band, which is consistently around the freezing level at 5 km height. Below the freezing level, liquid precipitation tends to attenuate the CPR signal, especially in the presence of moderate/heavy precipitation. In regions of strong attenuation where the surface return disappears (like for the profiles corresponding to the along-track distance between 1000 and 1200 km corresponding to the eye wall and the rain bands), the 2C-RAIN-PROFILE algorithm does not converge and the cumulative attenuation profile is retrieved down to 10 dB via the Hitschfeld and Bordan (1954) technique. All the segments of the profiles below such attenuation level (shaded region in Figure 2a) are excluded from the WIVERN reconstruction since they are deemed to be

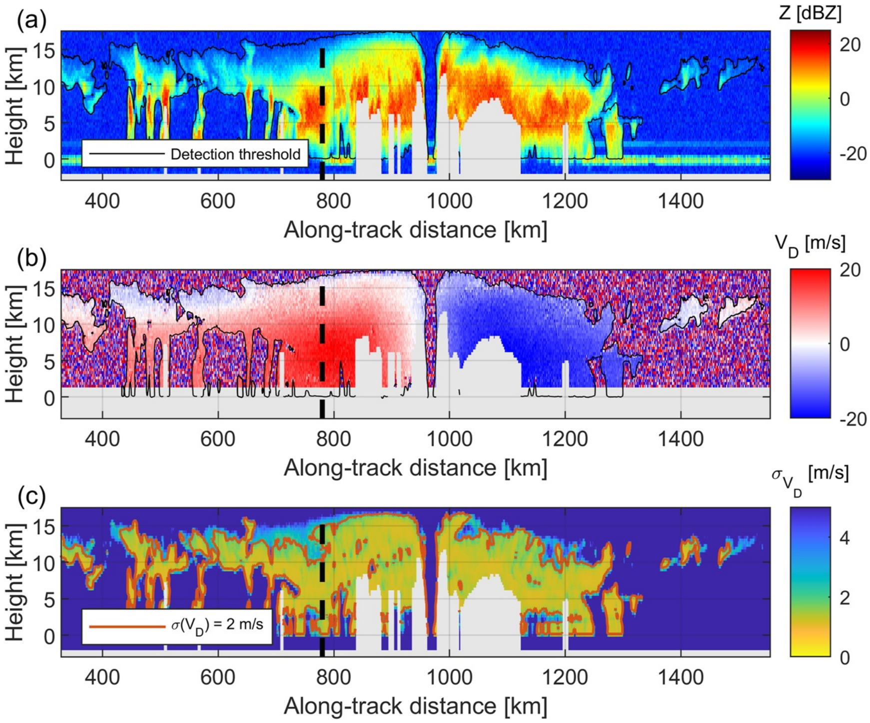

Figure 3. Simulated 1 km WIVERN (a) reflectivity curtain, (b) side-view Doppler velocity, and (c) expected Doppler velocity accuracy. The thin black lines in panels (a) and (b) show the contour of WIVERN detection threshold at 1 km resolution (−20 dBZ) and the orange line in panel (c) shows the contour of a Doppler velocity accuracy of 2 m s^{-1}. The black dash vertical line indicates the position of the profile illustrated in Figure 11.

adversely affected by vigorous convection, strong attenuation and multiple scattering. In the next section, we want to illustrate the simulation of WIVERN Doppler velocity in the side direction. Hence, cross-track LoS winds are displayed in Figure 2b. They roughly correspond to the zonal winds reduced by a factor $\sin\theta_i = 0.66$, with the typical wind direction inversion when going through the eye of the typhoon as expected from cyclonic circulation.

2.4. Simulation of WIVERN Observations of the Typhoon Choi-Wan

In Figure 1, the 800-km wide ground track of the WIVERN antenna boresight is illustrated on top of the MODIS visible image of Choi-Wan for 23 rotations. Note that the scanning pattern of the radar footprints (an ellipse with minor and major axis equal to 0.75 and 1 km, respectively) will provide an 8% coverage of the swath with gaps of the order of 20 km between successive footprints behind the satellite track (forward/backward views inset in Figure 1). On the contrary, there will be continuous coverage along the satellite direction at the swath edges (side view inset in Figure 1). The CloudSat reflectivity curtain of Figure 2a can be used for simulating the WIVERN observations in side view. This could indeed be the reconstructed curtain observed by WIVERN in the case its ground track was 400 km West of the CloudSat track, like in Figure 1.

The WIVERN observations simulated in side view at 1 km integration are shown in Figure 3. Most of the reflectivity features seen by the CloudSat radar are visible in WIVERN measurements. Because of the low number of independent pulses (8) and given its single pulse sensitivity of −15 dBZ, the reflectivity equivalent noise floor at 1 km will be −20 dBZ, hence the WIVERN radar will have a slightly reduced sensitivity compared to CloudSat (e.g., some of the high clouds below −20 dBZ in Figure 2 will not be detected by WIVERN). Note that recent industrial studies indicate that a better sensitivity of the WIVERN radar might be possible. In order to evaluate the effect of an improved sensitivity, several realistic values of reflectivity equivalent noise floor will be used in the simulations and the respective results will be presented in Section 3. Like for CloudSat, strong attenuation would be encountered in the heavy precipitation parts below the freezing level; this is why such regions have been whitened. Nevertheless, plenty of observations would be possible above the freezing level (i.e., roughly between 5 and 15 km height) both in the inner and outer core of the TC. Besides, the surface returns appear much

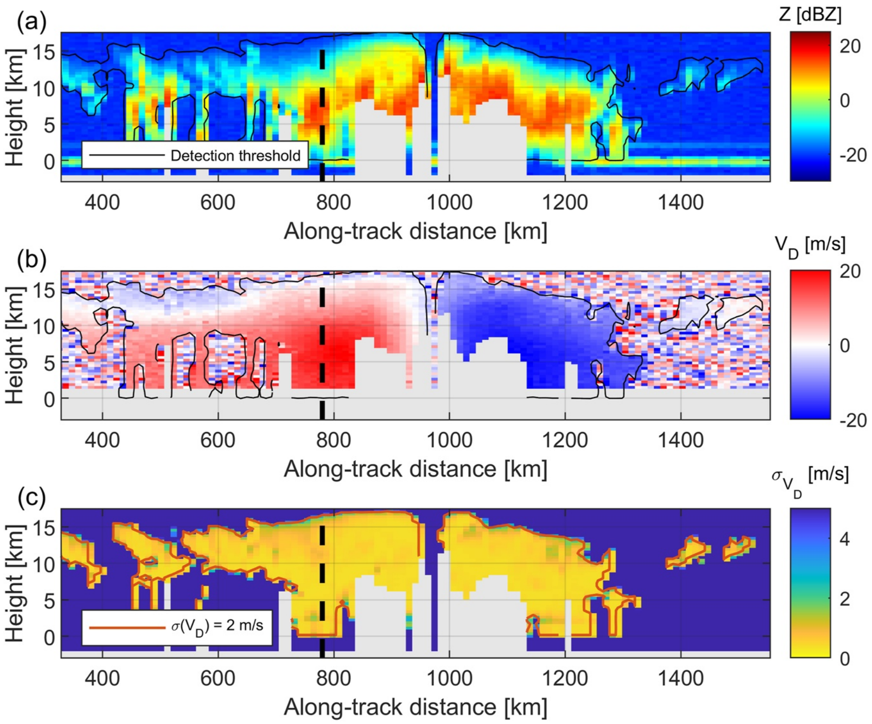

Figure 4. Same as Figure 3 but with 10 km averaging distance.

weaker compared to the CloudSat observations, a clear advantage over CloudSat for sampling low precipitating clouds. This is due to the significant reduction in the normalized backscattering cross sections of water surfaces when moving from nadir to 42° incidence angle (Battaglia et al., 2017).

According to the well established Doppler theory, the estimation of Doppler velocity improves with signal-to-noise ratio (SNR) and number of samples (i.e., with integration length). For the WIVERN specifics, the accuracy of LoS Doppler velocities measurements is expected to be better than 3 m s^{-1} for SNR >0 dB (for details, see Section 3.4.1 and Figure 10). At high SNR, the WIVERN LoS Doppler velocities measurements are expected to come with a maximum accuracy of about 1.1 m s^{-1} at 1 km resolution and 0.4 m s^{-1} at 10 km resolution. Of course, the resulting mean wind accuracy cannot be as good and will depend on the SNR distribution of the observed clouds. Other sources of errors such as NUBF and WS are discussed in Section 3.4. As noted in Section 2.2, it will be shown that these effects have a minor impact on Doppler velocity accuracy compared to the Doppler estimation (Figure 11).

The LoS Doppler velocities depicted in Figure 3b show increased noisiness when moving toward low SNRs. The accuracy of Doppler velocity shown in Figure 3c takes into account the SNR of the reflectivity measurements. For a spaceborne radar, the effect of range on SNR level is marginal within the sampling window, and hence, a threshold on SNR is a simple and efficient way to flag the quality of Doppler measurements. When SNR >0 (i.e., $Z > -15$ dBZ), the simulated Doppler velocity well reproduces the ECMWF fields with vast regions expected to have errors lower than 2 m s^{-1} (orange contour in Figure 3c). On the contrary, when SNR $\ll 0$, the Doppler velocity measurements become random numbers within the Nyquist interval (−40 to +40 m s^{-1} for $T_{HV} = 20$ μs). Additionally, in order to avoid issues with partial beam filling (e.g., in case of strongly reflective clouds with sharp edges), cloud edges will also need to be flagged. In all the typhoon regions above the freezing level and away from cloud edges, the wind estimates have a reasonable accuracy, demonstrating the great potential of WIVERN observations in characterizing simultaneously the microphysical and dynamical structure of TCs at sub-freezing temperatures.

In order to improve cloud detection and wind accuracy, WIVERN observations can be averaged over a longer integration length. An example with a 10 km averaging distance is shown in Figure 4. While Figure 4 shows fewer details than Figure 3, low reflective clouds are better detected (the area delimited by the detection threshold contour gets wider in Figure 4a). Furthermore, the improved sensitivity leads to more accurate Doppler velocity measurements and the regions where errors lower than 2 m s^{-1} are expected are clearly more extended. While averaging along the track is generally considered useful for reducing the noise error, it can be detrimental when averaging over distances where reflectivity and winds are not uniform either because of intensity or direction, for example, in regions with strong wind shears, or in the proximity of convective cores. In order to evaluate the effect of averaging, several averaging distances have been used in the simulations and the respective results are presented in Section 3.

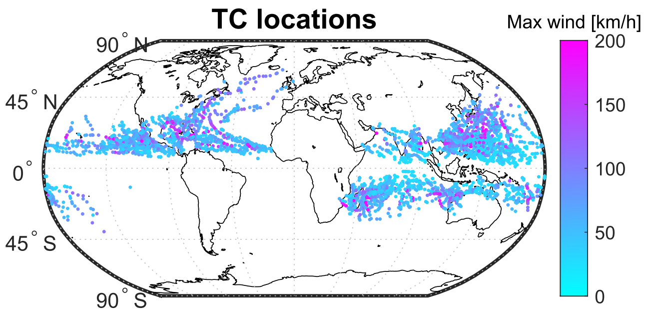

Figure 5. Location and maximum wind speed of all the tropical cyclones listed in the 2D-TC dataset for the years 2007, 2008, and 2009.

3. Statistical Analysis

3.1. The CloudSat TC Data Set

The CloudSat TC dataset includes CloudSat CPR intercepts of TCs within 1,000 km of the storm center for the period between 2 June 2006 till 31 December 2013 for a total of 10.6 million radar profiles (more than 170,000 within 100 km) (Tourville et al., 2015). The years 2007, 2008, and 2009 have been analyzed, representing the core of the dataset with respectively 1,244, 1,411, and 1,235 CloudSat overpasses (in comparison to the original dataset, we have excluded the overpasses where any of the CloudSat data product necessary for WIVERN simulation is missing, see Figure B1) of 263 different TCs (with an average of 15 overpasses per cyclone). According to the overall statistics from Tourville et al. (2015), CloudSat overpassed on average 4,331 TCs over the 2007–2009 period with 5.8 million (93 thousand) radar profiles at 1 km integration along track within 1000 km (100 km) from TC center corresponding to an average of 1.9 million/year (31 thousand/year).

Figure 5 shows the location and the maximum sustained 1-min wind speed of such storms as derived from the Automated Tropical Cyclone Forecasting System. The West Pacific basin region contains the greatest number of TC CPR intercepts (1,143) followed by the Southern Hemisphere (1,093), Atlantic (682), East Pacific (659), Indian Ocean (287), and Central Pacific (72) regions.

The contour frequency by altitude displays (CFAD) of the CloudSat reflectivity for the entire dataset (Figure 6a) demonstrates that TC systems are typically very tall, they exhibit large reflectivities with highest values typically between 5 and 8 km, regions of sharp increase of reflectivities with decreasing height in the upper troposphere and regions of large attenuation below the freezing level (always at about 5 km) as highlighted by the sloping of reflectivities toward lower values in the lower troposphere.

Figure 6b shows the cumulative distribution of CloudSat cloud types according to Sassen et al. (2008) classification, as function of height. Firstly, the total count of cloud peaks at about 0.3 million up to 14 km, meaning that about 16% of the profiles within 1,000 km from TC center are cloudy. Secondly, the eight cloud class distribution demonstrates that in TCs there is a mixture of cloud classes with a total of 32%, 9%, 5%, 4%, 7%, 21%, and 22%, respectively for deep convection, nimbostratus, cumulus, stratocumulus, altocumulus, altostratus, and cirrus clouds. Therefore, though deep convection represents a large percentage of the entire cloud cover, the majority of clouds are likely to be found in areas where up and downdraft will not modify significantly the horizontal wind estimates. These findings agree with previous research (Houze, 2010) that found a mixture of convective and stratiform precipitation (with the latter representing between 30% and 50% of the total) in the eyewall, inner core, and outer rainband region. In non-convective regions, WIVERN will be able to retrieve the horizontal LoS winds. However, it should be noted that the detection of convective up and downdraft in WIVERN observations will not be straightforward. Even if the convective regions are secondary and that it would only affect a small number of observations with a significant magnitude, this is a potential source of error which cannot be easily assessed in this study because the vertical wind is unknown. As a worst case scenario, we can consider that all the profiles classified as deep convection and cumulus clouds contain significant vertical winds, therefore reducing the number of accurate measurements by one third in the following statistical analysis.

Finally, the CFADS of ECMWF horizontal winds projected onto the LoS corresponding to the along and cross directions are shown in the bottom panels of Figure 6. Winds show maximum amplitudes around 9–12 km but very seldom exceed 40 m s^{-1} (7‰ in the cross direction, and a factor 1,000 less in the along direction).

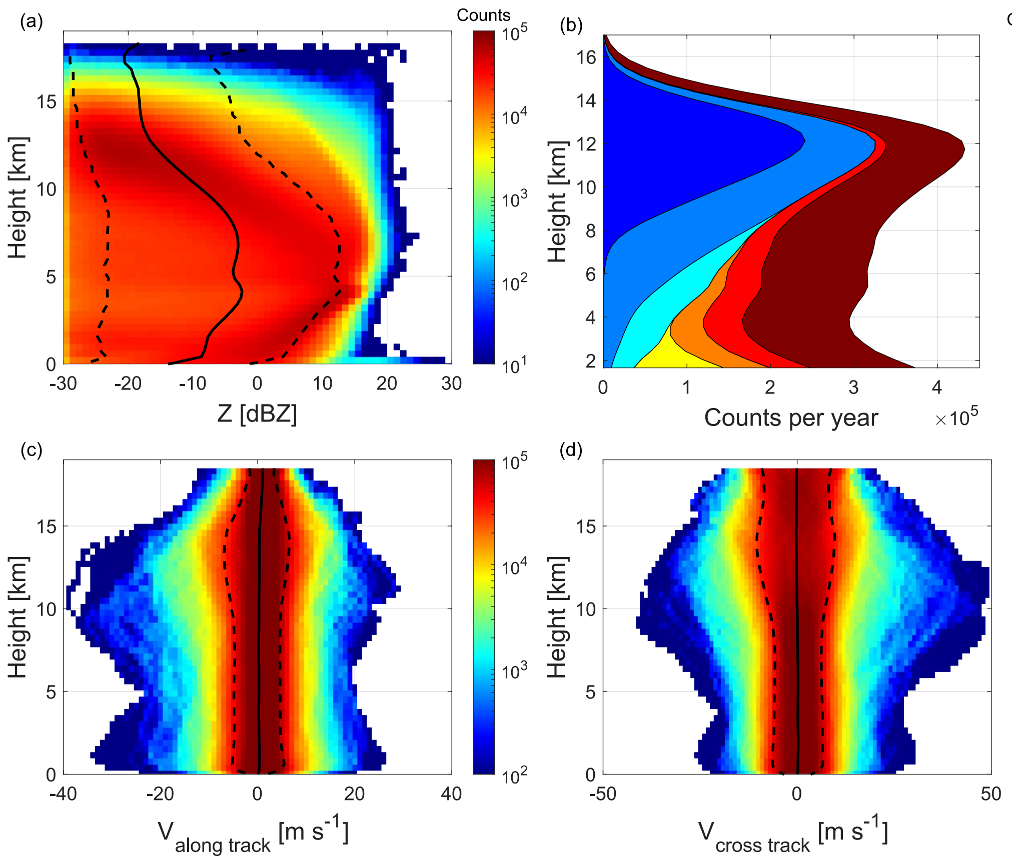

Figure 6. Top panels: reflectivity CFAD (a) and cloud class cumulative distribution as function of height (b). DC: deep convection; NS: nimbostratus; CU: cumulus; SC: stratocumulus; ST: stratus; AC: altocumulus; AS: altostratus; CI: cirrus. Bottom panels: WIVERN LoS along-track (c) and cross-track winds (d).

Therefore, with $T_{HV} = 20$ μs (corresponding to a Nyquist velocity of ±40 m s^{-1}), biasing due to the polarization diversity pulse pair estimation (see Section 3.4.1) is not expected to be a serious issue in WIVERN measurements.

3.2. WIVERN Cloud Measurements in TC

The procedure described in the flowchart of Figure B1 has been applied to the full 2007–2009 TC dataset. The first thing to establish is the impact of the slant-view and of the reduced sensitivity on the WIVERN capability in sensing clouds.

Even in intense precipitating systems such as TCs, the proportion of saturated profiles (where attenuation is so strong that attenuation correction of CloudSat reflectivity is not possible with good accuracy) is small in comparison to a large number of useful profiles. Figure 7a demonstrates that the reduction of data due to saturation is perceptible in CloudSat data only below 8 km (difference between the black and gray lines). The lower sensitivity of WIVERN causes a reduction of the cloud detection at all levels and increasingly deteriorates when assuming worse single pulse sensitivities (compare magenta, blue, and green lines).

Figure 8a shows the cloud detection with respect to the CloudSat reference as function of the distance from the TC center for the medium reflectivity equivalent noise floor at 1 km of −23 dBZ. The reduction of cloud detection due to saturated profiles or lower sensitivity clearly depends on the distance from the TC center. In particular, the eye walls (from 25 to 125 km from TC center) generally correspond to the heaviest rain rates and strongest attenuation (e.g., see the gray shading reaching the 10 km level at about 25 km from Choi-Wan

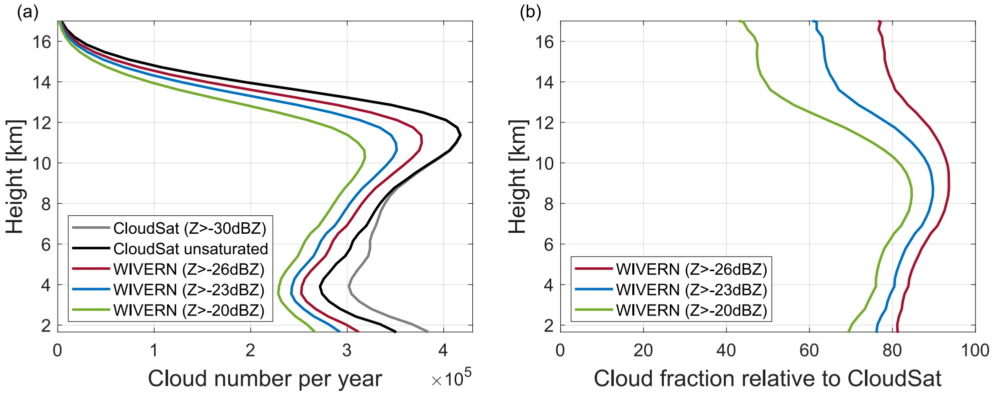

Figure 7. (a) Profiles of the annual number of clouds detected in TC by CloudSat or WIVERN with different detection limits as indicated in the legend. (b) Fraction of cloud detection relative to the CloudSat reference (gray line in the left panel) for three different WIVERN detection limits.

eye in Figure 2a) and, in this range, only about 65% of CloudSat clouds will be detected near the surface. Nevertheless, attenuation is generally not that strong in the ice phase (note that the typhoon Choi-Wan is an exceptional case) and the cloud detection relative to CloudSat will be about 90% between 6 and 11 km whatever the distance from storm center. Only a small but steady reduction of the cloud detection with the distance from TC center is found above 5 km (e.g., at 10 km, the cloud fraction reduces from 95% to 85% at 50–1,000 km from TC center, respectively). Such a reduction can be explained by the fact that, with the distance from TC centers, there is an increased frequency of thin clouds which are not detected by WIVERN due to its lower sensitivity.

Averaging over all distances from TC center, the cloud occurrence remains higher than 75% compared to the CloudSat reference for all levels between 3 and 11 km when adopting the baseline configuration of the reflectivity equivalent noise floor at 1 km of −20 dBZ (Figure 7b, green line). The reduction in cloud detectability is

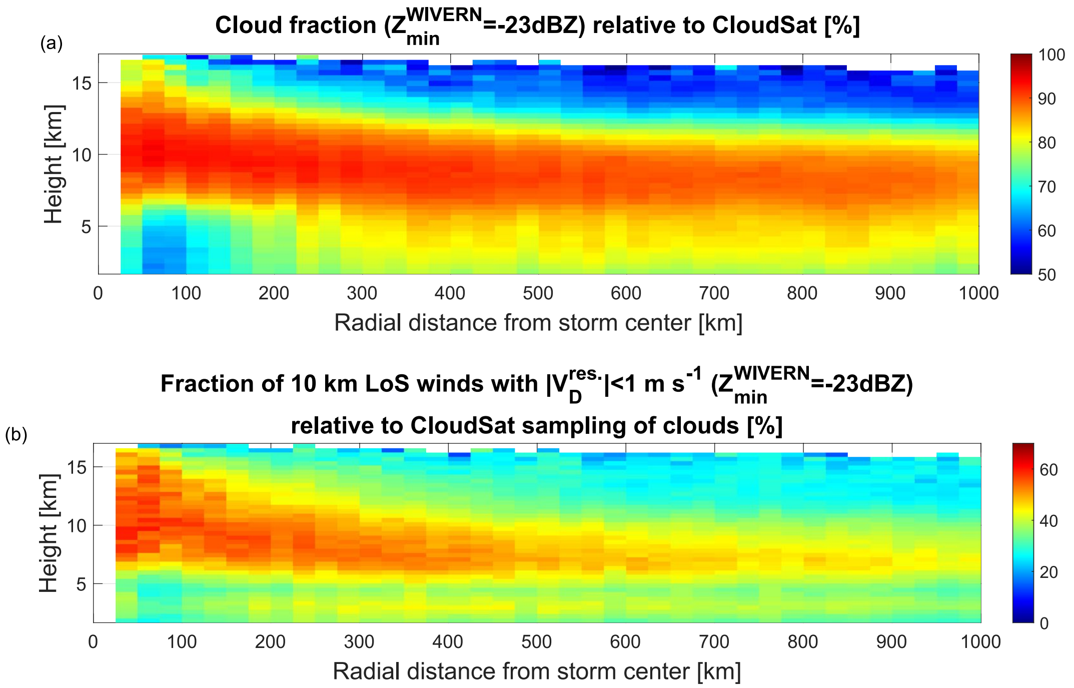

Figure 8. (a) Occurrence of 1 km cloud detection relative to the CloudSat reference, using a−23 dBZ sensitivity radar and as a function of the distance from TC center. (b) Occurrence of 10 km winds associated with an accuracy better than 1 m s^{-1} using a−23 dBZ sensitivity radar, relative to the CloudSat reference, and as a function of the distance from TC center.

limited to about 10% compared to the CloudSat reference if the detection limit is further improved toward −26 dBZ (magenta line).

Note that the CloudSat reference provides an average of about 0.35 million clouds at each level between 1 and 13 km in TC every year (i.e., roughly 9 million 1 km horizontally extended clouds in TC annually, when assuming 500 m layers). In a pure geometrical sense, WIVERN will sample 1,000 km radius weather features with a sampling rate 70 times larger than CloudSat (Appendix A). By taking into account its reduced (baseline) sensitivity, it will be 53 times more efficient than CloudSat for sampling TCs. Assuming layers of 650 m, we expect to detect about 350 million 1 km horizontally extended clouds in TC annually (exact computation from profiles of Figures 7a and 7b leads to 358 million).

3.3. WIVERN Wind Measurements in TCs

The second step is to estimate how many winds measurements better than a certain accuracy will be attainable from WIVERN. The accuracy of free troposphere horizontal wind observations required for improving global NWP is defined by the OSCAR (Observing Systems Capability Analysis and Review Tool) resource of the World Meteorological Organization (WMO) (WMO, 2023). Global wind observations at 100 km horizontal resolution, every 6 hr, and with an uncertainty of 3 m s^{-1} for horizontal wind vector (i.e., corresponding to the uncertainty of 1.4 m s^{-1} for WIVERN LoS Doppler velocity) are considered as a ”breakthrough”, but a ”goal” observing system would need to provide wind observations at a horizontal resolution as high as 15 km. Yet, even if measurements from Aeolus were associated with random errors larger than the ”breakthrough” recommendation from WMO, their impact on ECMWF global NWP system was nevertheless very positive (Rennie et al., 2021).

In a future study, an observing system experiment dedicated to WIVERN observations is necessary to determine the optimal accuracy and resolution required for data assimilation. For example, Sippel et al. (2014) showed a significant positive impact on a hurricane forecast by assimilating Doppler radar observations from a conically scanning airborne radar, but significant averaging of the high resolution Doppler velocity measurements was required to reach an accuracy suited to their assimilation.

In this section, statistics of LoS wind measurements with an accuracy of 1 and 3 m s^{-1} and at various resolutions will be derived. Realistic Doppler velocities that would be observed by WIVERN have been simulated for various reflectivity equivalent noise floors (20, −23, and −26 dBZ) and various integration lengths (1, 2, and 10 km). From the reflectivity and Doppler velocity gradients averaged over 1 × 5 km boxes, NUBF and WS errors corrections (Battaglia et al., 2023) provide unbiased velocity estimates which are compared to the LoS wind velocity, finally yielding the wind residual statistics. Results are similar for forward and side pointing (only the results for forward pointing are shown in Figures 8b and 9 for simplicity).

To start with, Figure 8b shows the occurrence of 10 km LoS winds associated with an accuracy better than 1 m s^{-1} using a −23 dBZ reflectivity equivalent noise floor, relative to the CloudSat reference, as a function of the distance from TC center. Like for cloud detection, most of the winds will be measured in the ice phase between 6 and 10 km. The significant reduction of the occurrence with the distance from TC center (e.g., at 8 km, the occurrence decreases from 60% to 40% at 50 and 1,000 km from TC center, respectively) is due to the increased frequency of clouds associated with lower reflectivity for which the Doppler measurements error increases. Indeed, as will be explained in Section 3.4, the accuracy of WIVERN winds measurements will depend mainly on the SNR level. Below the melting level, the proportion of winds is almost uniform over the distance from TC center, with a peak of 45% at the 3 km level. Only a modest minimum (roughly 30%) is found between 25 and 125 km from TC center.

Averaging over all distances from TC center, the occurrence of LoS winds that would be measured with an accuracy better than 1 m s^{-1} (3 m s^{-1}) compared to the CloudSat cloud detection is shown in Figure 9a (Figure 9b). As can be expected, the probability of useful Doppler velocity estimates raises with an increasing sensitivity of the 94 GHz radar onboard WIVERN and a longer integration length. In particular, the integration length is greatly valuable for enhancing the number of precise Doppler velocity estimates (i.e., better than 1 m s^{-1}, Figure 9a). When relaxing the required accuracy on the Doppler velocity (Figure 9b), the benefit is less evident and the fraction of useful winds reach a maximum of about 60% for an accuracy better than 5 m s^{-1} (not shown).

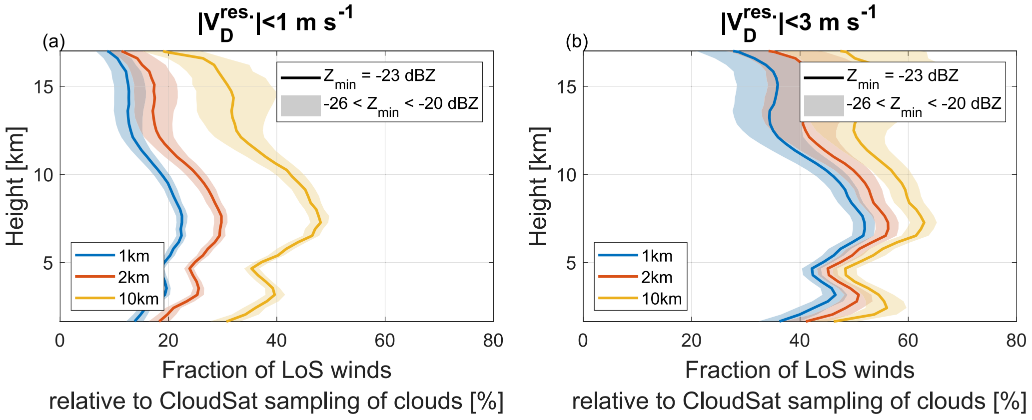

Figure 9. Profiles of the fraction of Doppler velocities as would be measured by WIVERN (relative to the CloudSat reference, gray line in Figure 7a) with an accuracy better than 1 (panel a) and 3 m s^{-1} (panel b) with averaging over 1 km, 2 and 10 km (see colors in legend) and different sensitivity levels.

Overall, the probability of useful Doppler velocity estimates (better than 3 m s^{-1}) will be around 45% up to about 11 km height and will peak around 3 and 7 km heights. Nevertheless, thanks to its 70 times better geometrical sampling (Appendix A), WIVERN would be 30 times more efficient than CloudSat if the latter were able to measure winds. Assuming layers of 650 m, this implies that WIVERN will measure about 200 million precise winds in TCs per year (the exact computation from profiles of Figures 7a and 9b leads to 194 million).

3.4. Sources of Error in WIVERN Wind Measurements

Different error sources can decrease the accuracy of WIVERN Doppler velocity. The advantage of running a simulator is that each error source can be evaluated separately. In the next sections, the different sources of errors are discussed and compared.

3.4.1. Errors Associated With the Polarization Diversity Pulse Pair (PDPP) Estimators

WIVERN reflectivities will be received in two H and V polarization channels. Cross-talk between the two channels will appear as low reflectivity ghosts 2.3 km above or below real targets (e.g., ghosts arising from surface cross-talk are visible in Figures 3a and 4a at around 2.3 km height as a horizontal line of low reflectivity standing out of the noise floor). While such ghosts will be generally easy to filter out in reflectivity measurements (Rizik et al., 2023), they will slightly increase the noise of the corresponding Doppler velocity according to the formula in Equation 1, without introducing any bias.

In this configuration, the computation of WIVERN Doppler velocities will be done via the polarization diversity pulse pair technique (Battaglia et al., 2022). Estimates of mean Doppler velocities from this technique are unbiased (apart when close to the Nyquist interval) and have an intrinsic noise associated with the phase and thermal noise (Pazmany et al., 1999). The precision of the Doppler measurements tends to improve with the correlation between the H and V pairs, the number of independent pulses that are averaged, higher levels of SNR (i.e., strong reflectivities), and signal-to-ghost ratio (SGR) (i.e., decreased contamination by ghosts). The standard deviation of the estimated Doppler velocity can be approximated as (Battaglia et al., 2022; Pazmany et al., 1999):

$$\sigma_{\hat{v}_D}^{PDPP} = \frac{1}{\sqrt{2N}}\frac{v_{Nyq}}{\pi\beta}\sqrt{\left(1+\frac{1}{\mathrm{SNR}}\right)^2+\frac{1}{\mathrm{SGR}_H}+\frac{1}{\mathrm{SGR}_V}+\frac{1}{\mathrm{SGR}_V\mathrm{SGR}_H}+\frac{1}{\mathrm{SNR}}\left(\frac{1}{\mathrm{SGR}_V}+\frac{1}{\mathrm{SGR}_H}\right)-\beta^2} \quad (1)$$

where:

$$\beta \equiv \rho_{HV}\, e^{-\frac{8\pi^2\sigma_v^2 T_{HV}^2}{\lambda^2}} \qquad v_{Nyq} \equiv \frac{\lambda}{4T_{HV}}$$

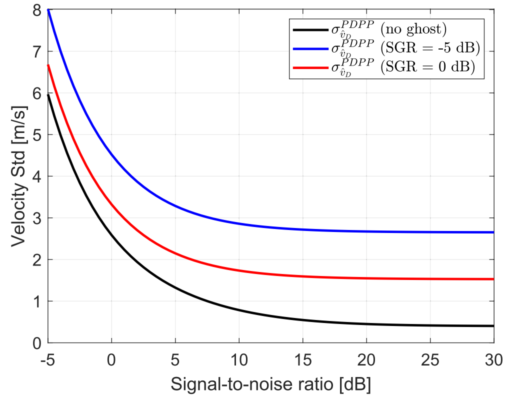

Figure 10. Doppler velocity standard deviation at $T_{HV} = 20$ μs and $\rho_{HV} = 1$ as a function of SNR, computed from the analytical formula in Equation 1 for different signal-to-ghost ratios (SGR) and for a 5 km integration (corresponding to 40 H-V pulse pairs). (1Note that for the baseline configuration, SNR = 0 dB corresponds to a reflectivity of −15 dBZ.

where λ is the radar wavelength and σ_v is the spectral width of the Doppler spectrum. ρ_{HV} accounts for the decorrelation between the H and V pulses which is the result of intrinsic decorrelation associated with the hydrometeors (i.e., decorrelation at lag-0) and decorrelation due to the backscattering volume mismatch, that is, to the fact that because of the antenna fast rotation, the two backscattering volumes for H and V pulses are not the same. The exponential term accounts for the time decorrelation due to the target reshuffling, which is proportional to λ/σ_v. Noise errors for a 5 km integration for different SNR levels are shown in Figure 10. The PDPP estimator is very robust even in case of spectral width broadening (e.g., due to large turbulence or hydrometeor fallspeed variation within the beam) like demonstrated in Figure 3, right panel of Battaglia et al. (2013).

3.4.2. Non-Uniform Beam Filling and Wind Shear Errors

Other sources of uncertainties are those due to reflectivity in-homogeneity within the backscattering volume and its coupling with the wind shear caused by the satellite motion (called Doppler fading or non-uniform beam filling (NUBF) bias, Tanelli et al., 2002) and with the atmospheric wind shear itself (hereafter named wind shear (WS) bias).

The mechanism for the generation of such errors is illustrated for a WIWERN forward-looking configuration in Figure 11, in which a beam of twice 3-dB illuminates the scene in correspondence to the profile highlighted with a vertical dashed black line in Figure 3. The corresponding NUBF and WS shear errors are shown in Figure 12, together with the residual error in Doppler velocity after applying the corrections described below.

For a fast-moving spaceborne Doppler radar, radar reflectivity gradients within the radar sampling volume can introduce a significant source of error in Doppler velocity estimates, that is, the NUBF errors (Tanelli et al., 2002). The Doppler velocity due to the satellite motion is first compensated for, according to the antenna boresight direction, and set to zero. Then the forward (backward) part of the backscattering volume appears to move upward (downward) as shown by the black contours in Figure 11. Across the beam of twice 3-dB, this velocity ranges from −6 to +6 m s^{-1}. When coupled with a reflectivity gradient, this satellite-motion-induced velocity shear can produce a bias. For instance, in the portion of the profile above (below) 6 km, the tendency of the reflectivity to increase (decrease) toward the surface produces an upward (downward) bias (see blue line in Figure 12).

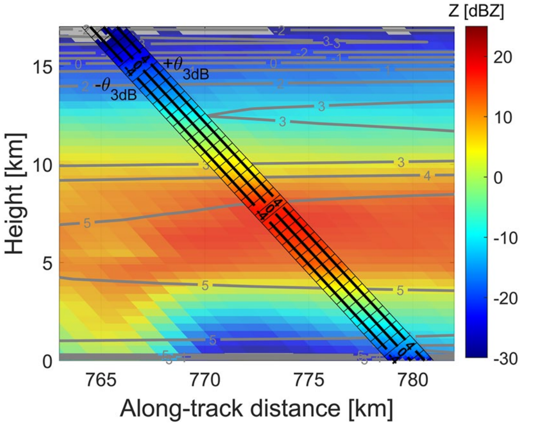

Figure 11. Illustration, in the forward direction configuration, of the sub-radar volume satellite-induced wind shear (as indicated by the black contour lines inside the antenna beam) and horizontal line-of-sight wind shear (values annotated in the gray contour lines) both in m s^{-1} for the profile at 780 km (dashed black lines) in Figure 3.

Wind shear errors occur when reflectivity and velocity gradients are present at the same time within the backscattering volume. In the current profile, there are no strong wind shears (maximum of few m s^{-1} km^{-1}), and therefore WS errors never exceed ± 0.2 m s^{-1} (purple line in Figure 12). As stated in Section 2.1, ECMWF is known to significantly underestimate vertical wind shear (Houchi et al., 2010). A better assessment of wind shear errors is possible by simulating WIVERN observations from the output of a cloud-resolving model, which is capable of producing realistic wind shear, vorticity and divergence features at scales of 1 km. This will be the focus of a separate study.

For nadir pointing radars, notional studies demonstrated that NUBF biases can be mitigated by estimating the along-track reflectivity gradient because NUBF-induced biases are, by definition, linearly proportional to such reflectivity gradients (Kollias et al., 2022; Schutgens, 2008; Sy et al., 2014). Similarly, in a slant-looking geometry, the relevant gradients are those along the direction orthogonal to the boresight and lying in the plane containing the satellite velocity and the antenna boresight direction (hereafter indicated as $\hat{\eta}$, Battaglia & Kollias, 2015). In a conically scanning system like WIVERN, it will be challenging to retrieve the Z-gradients along such directions and the correction will change according to the azimuthal scanning angle. For instance, when looking forward/backward, $\hat{\eta}$ is a combination of the vertical

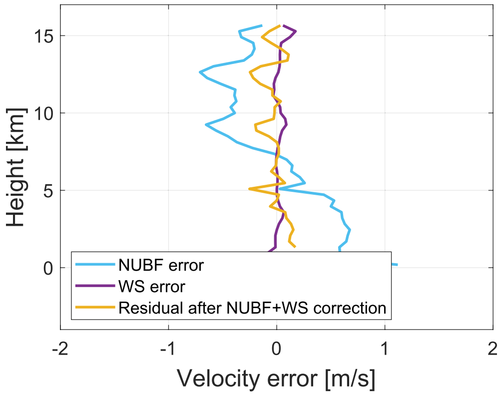

Figure 12. Demonstration of NUBF and WS bias corrections for the profile shown in Figure 11.

and of the horizontal along-track component, whereas when looking sideways, $\hat{\eta}$ coincides with the along-track direction.

For Gaussian circular antennas, if the reflectivity field can be approximated to vary linearly within the backscattering volume, then the bias introduced by the satellite motion is equal to (Battaglia & Kollias, 2015; Sy et al., 2014):

$$\Delta_{NUBF} = v_{sat}^{\perp BS} \frac{\nabla_{\hat{\eta}} Z}{4.343} \frac{1}{16\log(2)} r\theta_{3dB}^2 \tag{2}$$

where r is the range between the satellite and the ground along the boresight, and $v_{sat}^{\perp BS}$ is the ground-track satellite velocity orthogonal to the antenna boresight. The estimation of the reflectivity gradient along $\hat{\eta}$, $\nabla_{\hat{\eta}} Z$, is troublesome not only in the presence of noisy measurements but also because WIVERN will not sample reflectivities in all directions but will only produce a 2D slanted reflectivity curtain along the boresight track. Two extreme situations can be considered.

1. in side view, $\hat{\eta}$ coincides with the satellite trajectory so that $\nabla_{\hat{\eta}} Z$ can be properly estimated from the actual measurements and Equation 2 can be used exactly with $v_{sat}^{\perp BS} = v_{sat}$;
2. in the forward and backward view, only the effect of the vertical gradient of reflectivities can be accounted for (which is likely the most relevant one, apart from when hitting cloud edges). Although the vertical gradients are not properly sampled by the slanted WIVERN geometry they can be well estimated because they are expected to be quite homogeneous on a scale of the order of a few kilometers. Equation 2 then becomes:

$$\Delta_{NUBF}^{forward/backward} = v_{sat} \cos\theta_i \sin\theta_i \frac{\nabla_z Z}{4.343} \frac{r}{16\log(2)} \theta_{3dB}^2 \tag{3}$$

which for the WIVERN parameters corresponds to a bias of 0.077 m s^{-1} per dB km^{-1}.

3.4.3. Pointing Errors

Any mispointing in the knowledge of the antenna boresight decreases the accuracy of the Doppler velocity because errors are introduced when subtracting the component of the satellite velocity parallel to the antenna boresight, $v_{sat}^{\parallel BS}$, along the antenna boresight. Different techniques to mitigate these errors are currently under study and are expected to contribute less than 0.3 m s^{-1} (Scarsi et al., 2023).

3.4.4. Error Budget

The WIVERN simulator developed in this study allows to evaluate the contribution from each source of error separately. For instance, the satellite motion NUBF-induced errors can be evaluated by computing the velocities running the simulator with or without satellite motion and then taking the differences between the two.

Using the TC dataset in forward view, the profiles of the relative contribution of pulse pair estimator, NUBF, and WS are shown in Figure 13 for 1 and 5 km integration lengths. At 1 km integration, the error from the pulse pair estimator is clearly the dominant term. It is maximum near cloud top where the SNR is low and is enhanced at around 2 km height where the surface's ghost generally degrades the accuracy of the wind. The next contributor is the NUBF error and its correction is clearly efficient with a decrease of the error by a factor of 1.5 on average. The correction of WS error on the other hand does not appear to be successful. Its contribution is negligible compared to the two other terms but might be underestimated due to the coarse resolution of ECMWF winds. More work is needed to fully assess the performances of the NUBF and WS corrections using for example, high-resolution data from cloud-resolving model outputs.

As expected when averaging over longer integration lengths, the apparent SNR increases and the pulse pair estimator error reduces substantially. Conversely, the contribution of NUBF and WS is only weakly affected by

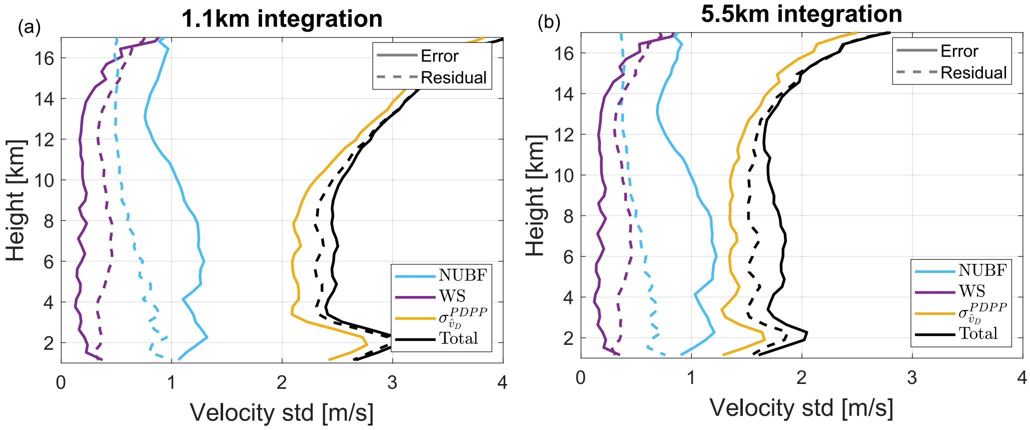

Figure 13. Profiles of the contribution from the main error sources (NUBF, WS, pulse pair estimator, see legend) on the Doppler velocity standard deviation at (a) 1 km and (b) 5 km integration. Dashed lines show the residual errors after the correction of NUBF and WS contribution as described in Section 3.4.2.

the noise level. For integration length larger than 10 km (not shown), the pulse pair estimator error starts to be dominated by the NUBF error, and the correction of the latter becomes essential.

4. Summary and Conclusions

The conically scanning Doppler W-band radar of the EE11 candidate WIVERN mission could provide for the first time global detailed observations of both the vertical structure of cloud and precipitation microphysics and, simultaneously, of the kinematic structure of the inner part of TCs.

Our study demonstrates that, despite the short wavelength of the radar (3 mm) which causes strong attenuation in the presence of large amounts of liquid hydrometeors, the system can profile most of the TCs, particularly the cloudy areas above the freezing level and the precipitating stratiform regions. Because of its lower sensitivity, the WIVERN radar would provide 75% observations of clouds and 45% accurate horizontal winds in TCs in comparison to CloudSat sampling of clouds, if it had the same sampling pattern. But thanks to its scanning antenna, WIVERN would actually provide 53 times more observations of clouds than CloudSat in TCs (30 times more observations of horizontal winds in comparison to CloudSat sampling of clouds). This will correspond to 358 million observations of clouds and 194 million observations of accurate winds every year inside TC if WIVERN is launched.

At 1 km integration, the uncertainty of horizontal wind measurements will be dominated by the intrinsic noise associated with Doppler radar measurements and will be around 3 m s^{-1}. When averaging the measurements over longer integration lengths this uncertainty decreases to for example, 1.5 m s^{-1} at 5 km integration. From 10 km integration, the error due to the wind shear caused by the satellite motion starts to be dominant and can be corrected by about a half. Other sources of error such as actual wind shear error or averaging error cannot be addressed satisfactorily with the CloudSat data because ECMWF winds are defined over a too coarse resolution. They will be the focus of further studies based, for example, on the output of sub-km resolution cloud-resolving model capable of producing realistic wind shear, vorticity and divergence features.

Observations from WIVERN would complement the sparse observations from aircraft-reconnaissance measurements and by ground-based and airborne Doppler radars. These measurements should shed new light on the interaction between the inner TC core and the storm environment, for example, thanks to a better understanding of the development of TC via the release of latent heat and the formation of precipitation.

It is also expected that the assimilation of these novel wind measurements will improve NWP's TC forecasts as already demonstrated for other microwaves active (Okamoto et al., 2016) and passive observations (Duncan et al., 2022; Zhang et al., 2021). Future work should assess the impact of the assimilation of WIVERN observations on the forecast of TC track, structure, intensity and rainfall.

Appendix A: WIVERN Versus CloudSat Sampling of TC

In order to determine how much better WIVERN will sample TCs compared to CloudSat, a dedicated study has been performed in this appendix. The principle is to compute the ratio between the length of the CloudSat radar boresight intersection with a hurricane, and the length of the WIVERN radar boresight intersection for the same overpass. Indeed, if the intersection of a nadir pointing system (like the CloudSat radar) with the hurricane is known, it is possible to retrieve what would be the length of the WIVERN radar intersection for the same overpass assuming that the two systems have the same orbit. More precisely, for a 1,000 km radius hurricane with its center located at specific longitude and latitude, the length of the CloudSat and WIVERN radars boresight groundtrack intersecting the hurricane can be computed based on their orbit and scanning geometry. An example of the methodology is presented in Figure A1.

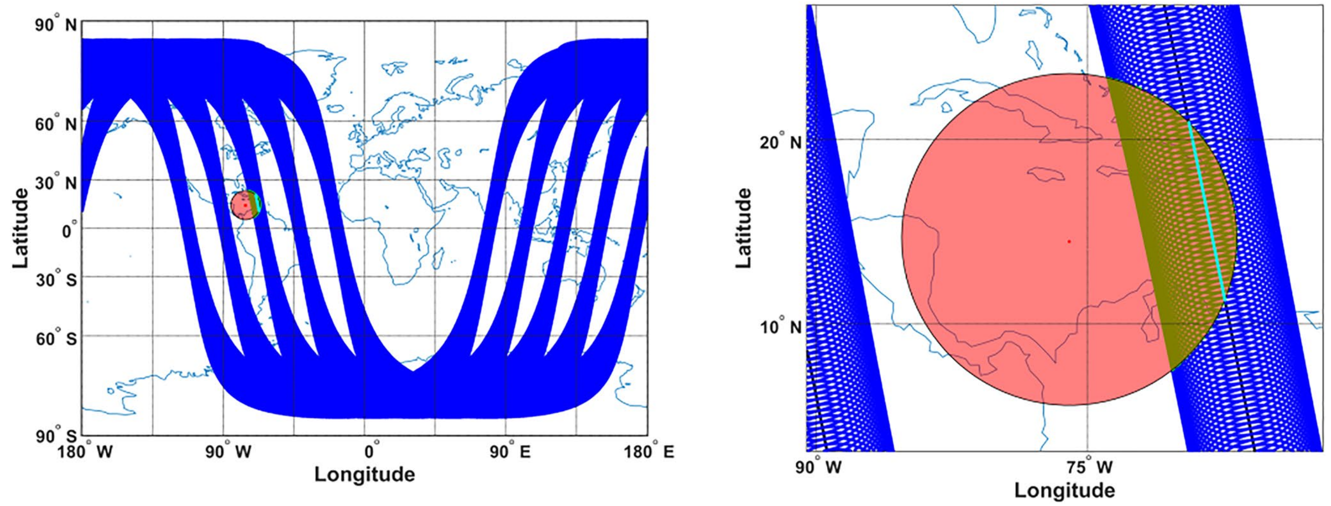

Figure A1. (a) Groundtrack (blue line) of the WIVERN radar boresight over five orbits, with the middle one intersecting a 1000 km radius circle representing a hurricane (in red). (b) Zoom on the hurricane, with the intersections of the WIVERN satellite groundtrack (representing intersection of the CloudSat radar since it is pointing toward nadir) and the WIVERN radar boresight intersection highlighted by the cyan and green lines, respectively.

Results have been averaged over 20 days of orbits with the center of the TC moved across the latitudinal band between 0° and 30°. The ratio between WIVERN and CloudSat sampling ranges from a minimum of 68 to a maximum of 74 with a mean value of 71.3. This demonstrates that the pure WIVERN geometrical sampling of TCs is about 70 times better than CloudSat. If we account for an 75% efficiency of WIVERN cloud detection compared to CloudSat (Figure 7b), this results in WIVERN being 53 times more efficient in sampling TCs.

Appendix B: Simulating WIVERN From CloudSat and ECMWF Winds

The simulation methodology is sketched in Figure B1. As it was already described in detail in Battaglia et al. (2018), only the main features are summarized below.

- First, the 94 GHz effective reflectivity, Z_{eff} (expressed in dBZ), and extinction coefficient, K_{ext} (expressed in dB m^{-1}), profiles are loaded from the 2C-RAIN-PROFILE (Haynes et al., 2009) product over ocean for the 2D CloudSat curtain. The derivation of the attenuation profile in the 2B-GEOPROF (Mace et al., 2007) product is based on the path integrated attenuation computed by the surface reference technique (Meneghini et al., 2000); this is only applicable over ocean without sea-ice. Over land, over sea-ice, and for strongly attenuated profiles over ocean, the profiles of extinction are partially reconstructed with the Hitschfeld and Bordan (1954) technique. The measured reflectivity Z_{co} (expressed in dBZ) at a range r in the WIVERN slant geometry accounts for the increased cumulative attenuation compared to the nadir-looking view:

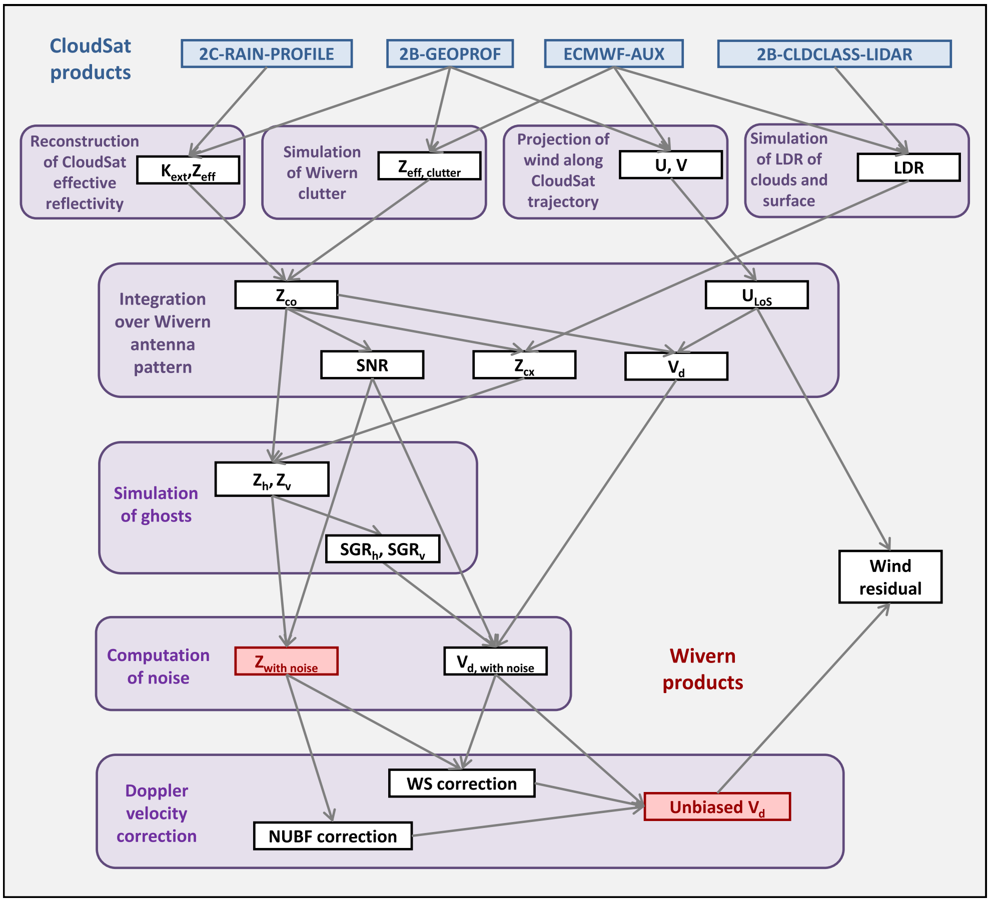

Figure B1. Flowchart describing the procedure to simulate WIVERN observations starting from CloudSat CPR observations and ECMWF reanalysis winds.

$$Z_{co}(r) = Z_{eff}(r) - 2\int_0^r K_{ext}(s)\,ds \tag{B1}$$

where the integral is carried out along the slant direction. The surface clutter position is derived from the 2B-GEOPROF product and modulated to the different WIVERN incidence angle according to airborne observations (Battaglia et al., 2017).

- Linear depolarization ratio (LDR, expressed in dB) values are reconstructed according to the temperature and the cloud type based on the 2B-CLDCLASS-LIDAR classification (Sassen et al., 2008): a climatology of the linear depolarization ratio profiles as a function of temperature has been derived from data collected at the Chilbolton observatory during a specific field campaign when the W-band Galileo polarimetric radar was pointing at 45° elevation angle in June and July 2017. The resulting profiles of the tenth, 25th, 50th, 75th and 90th percentiles are shown in Figure B2. LDR values are reconstructed from the climatological quantiles assuming normal distributions with mean value and standard deviation depending on the cloud class and temperature range following Table B1. Since the LDR values are only needed for simulating the cross-talk effects, this approach is deemed sufficient for demonstrating the climatological impact of the ghosts on Doppler velocity accuracy. From profiles of Z_{co} and LDR, profiles of cross-polar reflectivities are computed as:

$$Z_{cx}(r) = Z_{co}(r) + \mathrm{LDR}(r). \tag{B2}$$

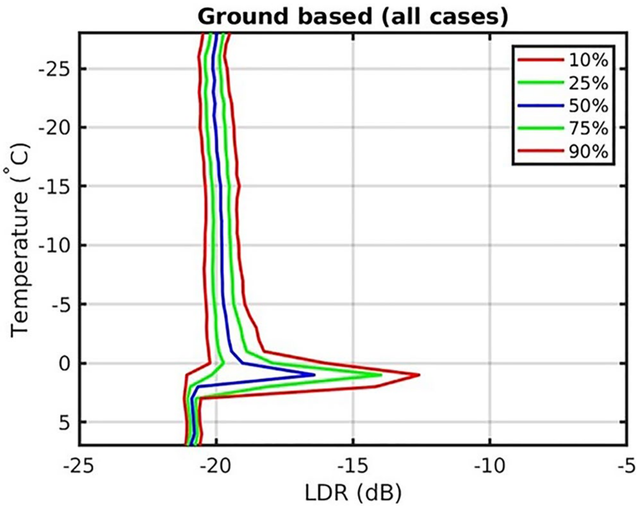

Figure B2. Dependence of LDR on temperature from W-band Galileo radar observations at Chilbolton and corresponding ECMWF temperature profiles (courtesy of John Nicol, Weather Radar New Zealand). Note the bad isolation between the co- and cross-polar channels of the radar, which leads to an overestimation of the LDR in rain.

Note that the W-band Galileo radar has antenna cross talks of the order of −23 dB, which leads to an overestimation of the climatological LDR of rain. This results in pessimistic estimates of the influence of ghosts: there will be less cross-talk in the real observations of the WIVERN radar whose isolation is expected to be −28 dB.

- Vertical profiles of the line of sight (LoS) winds geo-located with CloudSat curtain are computed by projecting ECMWF horizontal winds from the ECMWF-AUX product onto the LoS; both along track and cross track winds are examined for simulating the ”forward” and the ”side” views.
- WIVERN reflectivities received in the two polarization channels, H and V, are simulated by taking into account the polarization diversity pulse-scheme (see Figure 1 in Battaglia et al. (2013)). Intrinsic to such a scheme, there is cross-talk between the two channels (also referred to as ghosts) and separated in range by $\Delta r_{T_{HV}} = cT_{HV}/2$, T_{HV} being the separation between the two pulses:

$$Z_H[r] = Z_{co}[r] + Z_{cx}\left[r - \Delta r_{T_{HV}}\right] \tag{B3}$$

$$Z_V[r] = Z_{co}[r] + Z_{cx}\left[r + \Delta r_{T_{HV}}\right] \tag{B4}$$

the H being the polarization of the first pulse of the pair sequence.

- All quantities are integrated over the WIVERN antenna pattern and convolved with the point target response function to simulate the antenna weighted co-polar reflectivity, $\langle Z_{co}\rangle_W$, the cross-polar reflectivity, $\langle Z_{cx}\rangle_W$ and the Doppler velocity, $\langle v_d\rangle_W$.
- Signal-to-ghost ratios (SGR) are computed as:

$$\mathrm{SGR}_H[r] \equiv \frac{\langle Z_{co}[r]\rangle_W}{\left\langle Z_{cx}\left[r - \Delta r_{T_{HV}}\right]\right\rangle_W} \tag{B5}$$

Table B1
Mean Value and Standard Deviation of LDR According to Cloud Class

Cloud class	Temperature [°C]	Mean LDR [dB]	σ_{LDR} [dB]
Ice	$T < -35$	−19	1.5
Mixed	$-35 < T < -1$	−17	1.5
Melting	$-1 < T < 4$	−14	1.5
Rain	$T > 3$	−21	2

$$\mathrm{SGR}_V[r] \equiv \frac{\langle Z_{co}[r] \rangle_W}{\left\langle Z_{cx}\left[r + \Delta r_{T_{HV}}\right] \right\rangle_W} \tag{B6}$$

- Instrument noise and stochastic noise are added to the reflectivities and to the Doppler velocities according to the procedure described in Battaglia et al. (2022). In order to evaluate the effect of the sensitivity of the WIVERN radar, different reflectivity equivalent noise floors at 1 km are used: −20, −23, and −26 dBZ.
- Doppler velocity corrections are implemented both for non-uniform beam filling (NUBF) and for wind shear (WS) according to the procedure described in Battaglia et al. (2018).

Data Availability Statement

The CloudSat tropical cyclone overpass data set is available at https://adelaide.cira.colostate.edu/tc/ website.

Acknowledgments

We thank Matthew Lebsock, Alain Protat and a third anonymous reviewer for their comments which helped greatly to improve the manuscript. This research has been supported by the European Space Agency under the activities ”WInd VElocity Radar Nephoscope (WIVERN) Phase 0 Science and Requirements Consolidation Study” (ESA Contract Number 4000136466/21/NL/LF) and ”End-to-End Performance Simulator Activity of the WIVERN Mission” (ESA Contract Number 4000139446/22/NL/SD). This research used the Mafalda cluster at Politecnico di Torino. The work of A. Rizik and F. Tridon were funded by Compagnia di San Paolo, Turin, Italy.

References

Battaglia, A., Dhillon, R., & Illingworth, A. (2018). Doppler W-band polarization diversity space-borne radar simulator for wind studies. *Atmospheric Measurement Techniques*, *11*(11), 5965–5979. https://doi.org/10.5194/amt-11-5965-2018

Battaglia, A., & Kollias, P. (2015). Error analysis of a conceptual cloud Doppler stereoradar with polarization diversity for better understanding space applications. *Journal of Atmospheric and Oceanic Technology*, *32*(7), 1298–1319. https://doi.org/10.1175/JTECH-D-14-00015.1

Battaglia, A., Martire, P., Caubet, E., Phalippou, L., Stesina, F., Kollias, P., & Illingworth, A. (2022). End to end simulator for the wivern w-band Doppler conically scanning spaceborne radar. *Atmospheric Measurement Techniques*, *2021*, 1–31. https://doi.org/10.5194/amt-2021-342

Battaglia, A., Scarsi, F. E., Mroz, K., & Illingworth, A. (2023). In-orbit cross-calibration of millimeter conically scanning spaceborne radars. *Atmospheric Measurement Techniques*, *16*(12), 3283–3297. https://doi.org/10.5194/amt-16-3283-2023

Battaglia, A., Tanelli, S., Kobayashi, S., Zrnic, D., Hogan, R. J., & Simmer, C. (2010). Multiple-scattering in radar systems: A review. *Journal of Quantitative Spectroscopy and Radiative Transfer*, *111*(6), 917–947. https://doi.org/10.1016/j.jqsrt.2009.11.024

Battaglia, A., Tanelli, S., & Kollias, P. (2013). Polarization diversity for millimeter spaceborne Doppler radars: An answer for observing deep convection? *Journal of Atmospheric and Oceanic Technology*, *30*(12), 2768–2787. https://doi.org/10.1175/JTECH-D-13-00085.1

Battaglia, A., Wolde, M., D'Adderio, L. P., Nguyen, C., Fois, F., Illingworth, A., & Midthassel, R. (2017). Characterization of surface radar cross sections at W-band at moderate incidence angles. *IEEE Transactions of Geoscience Remote Sensing*, *55*(7), 3846–3859. https://doi.org/10.1109/TGRS.2017.2682423

Bond, N. A., Cronin, M. F., Sabine, C., Kawai, Y., Ichikawa, H., Freitag, P., & Ronnholm, K. (2011). Upper ocean response to typhoon choi-wan as measured by the kuroshio extension observatory mooring. *Journal of Geophysical Research*, *116*(C2), C02031. https://doi.org/10.1029/2010JC006548

Bucci, L. R., Majumdar, S. J., Atlas, R., Emmitt, G. D., & Greco, S. (2021). Understanding the response of tropical cyclone structure to the assimilation of synthetic wind profiles. *Monthly Weather Review*, *149*(6), 2031–2047. https://doi.org/10.1175/MWR-D-20-0153.1

Cordoba, M., Dance, S. L., Kelly, G. A., Nichols, N. K., & Waller, J. A. (2017). Diagnosing atmospheric motion vector observation errors for an operational high-resolution data assimilation system. *Quarterly Journal of the Royal Meteorological Society*, *143*(702), 333–341. https://doi.org/10.1002/qj.2925

Cui, Z., Pu, Z., Tallapragada, V., Atlas, R., & Ruf, C. S. (2019). A preliminary impact study of cygnss ocean surface wind speeds on numerical simulations of hurricanes. *Geophysical Research Letters*, *46*(5), 2984–2992. https://doi.org/10.1029/2019GL082236

Didlake, A. C., Heymsfield, G. M., Reasor, P. D., & Guimond, S. R. (2017). Concentric eyewall asymmetries in hurricane gonzalo (2014) observed by airborne radar. *Monthly Weather Review*, *145*(3), 729–749. https://doi.org/10.1175/mwr-d-16-0175.1

Duncan, D. I., Bormann, N., Geer, A. J., & Weston, P. (2022). Assimilation of amsu-a in all-sky conditions. *Monthly Weather Review*, *150*(5), 1023–1041. https://doi.org/10.1175/mwr-d-21-0273.1

Emanuel, K. (2001). Contribution of tropical cyclones to meridional heat transport by the oceans. *Journal of Geophysical Research*, *106*(D14), 14771–14781. https://doi.org/10.1029/2000JD900641

Emanuel, K. (2003). Tropical cyclones. *Annual Review of Earth and Planetary Sciences*, *31*(1), 75–104. https://doi.org/10.1146/annurev.earth.31.100901.141259

Emanuel, K. (2021). Response of global tropical cyclone activity to increasing co2: Results from downscaling cmip6 models. *Journal of Climate*, *34*(1), 57–70. https://doi.org/10.1175/JCLI-D-20-0367.1

Fabry, F. (2015). *Radar meteorology: Principles and practice*. Cambridge University Press. https://doi.org/10.1017/CBO9781107707405

Feng, J., Duan, Y., Sun, W., & Zhou, Y. (2023). Sensitivity analysis of assimilating Doppler radar radial winds within the inner- and outer-core regions of tropical cyclones. *Journal of Geophysical Research: Atmospheres*, *128*(8), e2022JD037583. https://doi.org/10.1029/2022jd037583

George, G., Halloran, G., Kumar, S., Rani, S. I., Bushair, M., Jangid, B. P., et al. (2021). Impact of aeolus horizontal line of sight wind observations in a global nwp system. *Atmospheric Research*, *261*, 105742. https://doi.org/10.1016/j.atmosres.2021.105742

George, J. E., & Gray, W. M. (1976). Tropical cyclone motion and surrounding parameter relationships. *Journal of Applied Meteorology and Climatology*, *15*(12), 1252–1264. https://doi.org/10.1175/1520-0450(1976)015<1252:tcmasp>2.0.co;2

Guimond, S. R., Reasor, P. D., Heymsfield, G. M., & McLinden, M. M. (2020). The dynamics of vortex rossby waves and secondary eyewall development in hurricane matthew (2016): New insights from radar measurements. *Journal of the Atmospheric Sciences*, *77*(7), 2349–2374. https://doi.org/10.1175/jas-d-19-0284.1

Haynes, J. M., L'Ecuyer, T. S., Stephens, G. L., Miller, S. D., Mitrescu, C., Wood, N. B., & Tanelli, S. (2009). Rainfall retrieval over the ocean with spaceborne W-band radar. *Journal of Geophysical Research Atmospheres*, *114*(D8), D00A22. https://doi.org/10.1029/2008jd009973

Hitschfeld, W., & Bordan, J. (1954). Errors inherent in the radar measurement of rainfall at attenuating wavelengths. *Journal of Meteorology*, *11*(1), 58–67. https://doi.org/10.1175/1520-0469(1954)011<0058:eiitrm>2.0.co;2

Houchi, K., Stoffelen, A., Marseille, G. J., & Kloe, J. D. (2010). Comparison of wind and wind shear climatologies derived from high-resolution radiosondes and the ECMWF model. *Journal of Geophysical Research*, *115*(D22123), D22123. https://doi.org/10.1029/2009JD013196

Houze, R. A. (2010). Clouds in tropical cyclones. *Monthly Weather Review*, *138*(2), 293–344. https://doi.org/10.1175/2009mwr2989.1

Illingworth, A. J., Barker, H. W., Beljaars, A., Ceccaldi, M., Chepfer, H., Clerbaux, N., et al. (2015). The EarthCARE satellite: The next step forward in global measurements of clouds, Aerosols, precipitation, and radiation. *Bulletin of American Meteorological Society*, *96*(8), 1311–1332. https://doi.org/10.1175/BAMS-D-12-00227.1

Illingworth, A. J., Battaglia, A., Bradford, J., Forsythe, M., Joe, P., Kollias, P., et al. (2018). Wivern: A new satellite concept to provide global in-cloud winds, precipitation, and cloud properties. *Bulletin of American Meteorological Society*, *99*(8), 1669–1687. https://doi.org/10.1175/BAMS-D-16-0047.1

Judt, F., & Chen, S. S. (2016). Predictability and dynamics of tropical cyclone rapid intensification deduced from high-resolution stochastic ensembles. *Monthly Weather Review*, *144*(11), 4395–4420. https://doi.org/10.1175/mwr-d-15-0413.1

Klotzbach, P. J., Bowen, S. G., Pielke, R., & Bell, M. (2018). Continental u.s. hurricane landfall frequency and associated damage: Observations and future risks. *Bulletin of American Meteorological Society*, *99*(7), 1359–1376. https://doi.org/10.1175/bams-d-17-0184.1

Knutson, T. R., McBride, J. L., Chan, J., Emanuel, K., Holland, G., Landsea, C., et al. (2010). Tropical cyclones and climate change. *Nature Geoscience*, *3*(3), 157–163. https://doi.org/10.1038/ngeo779

Kollias, P., Puidgomènech Treserras, B., Battaglia, A., Borque, P., & Tatarevic, A. (2022). Processing reflectivity and Doppler velocity from earthcare's cloud profiling radar: The c-fmr, c-cd and c-apc products. *EGUsphere*, 1–25. https://doi.org/10.5194/egusphere-2022-1284

Laroche, S., & St-James, J. (2022). Impact of the aeolus level-2b horizontal line-of-sight winds in the environment and climate change Canada global forecast system. *Quarterly Journal of the Royal Meteorological Society*, *148*(745), 2047–2062. https://doi.org/10.1002/qj.4300

Leidner, S. M., Annane, B., McNoldy, B., Hoffman, R., & Atlas, R. (2018). Variational analysis of simulated ocean surface winds from the cyclone global navigation satellite system (cygnss) and evaluation using a regional osse. *Journal of Atmospheric and Oceanic Technology*, *35*(8), 1571–1584. https://doi.org/10.1175/JTECH-D-17-0136.1

Lemaître, Y., & Viltard, N. (2013). 3D wind field from spaceborne Doppler radar. In R. Meynart, S. P. Neeck, & H. Shimoda (Eds.), *Sensors, systems, and next-generation satellites xvii* (Vol. 8889, p. 88891L). SPIE. https://doi.org/10.1117/12.2028864

Mace, G. G., Marchand, R., Zhang, Q., & Stephens, G. (2007). Global hydrometeor occurrence as observed by CloudSat: Initial observations from summer 2006. *Geophysical Research Letters*, *34*(9), L09808. https://doi.org/10.1029/2006GL029017

Marinescu, P. J., Cucurull, L., Apodaca, K., Bucci, L., & Genkova, I. (2022). The characterization and impact of aeolus wind profile observations in noaa's regional tropical cyclone model (hwrf). *Quarterly Journal of the Royal Meteorological Society*, *148*(749), 3491–3508. https://doi.org/10.1002/qj.4370

Matrosov, S. Y., Battaglia, A., & Rodriguez, P. (2008). Effects of multiple scattering on attenuation-based retrievals of stratiform rainfall from CloudSat. *Journal of Atmospheric and Oceanic Technology*, *25*(12), 2199–2208. https://doi.org/10.1175/2008JTECHA1095.1

Meneghini, R., Iguchi, T., Kozu, T., Liao, L., Okamoto, K., Jones, J. A., & Kwiatkowski, J. (2000). Use of the surface reference technique for path attenuation estimates from the TRMM precipitation radar. *Journal of Applied Meteorology*, *39*(12), 2053–2070. https://doi.org/10.1175/1520-0450(2001)040<2053:uotsrt>2.0.co;2

Moore, R., Beh, B., & Song, S. (1996). Scanning for a satellite radar wind sounder (raws). *Igarss '96. 1996 International Geoscience and Remote Sensing Symposium*, *2*, 96–998. https://doi.org/10.1109/IGARSS.1996.516546

Okamoto, K., Aonashi, K., Kubota, T., & Tashima, T. (2016). Experimental assimilation of the gpm core observatory dpr reflectivity profiles for typhoon halong (2014). *Monthly Weather Review*, *144*(6), 2307–2326. https://doi.org/10.1175/MWR-D-15-0399.1

Pazmany, A. L., Galloway, J. C., Mead, J. B., Popstefanija, I., McIntosh, R. E., & Bluestein, H. W. (1999). Polarization diversity pulse-pair technique for millimeter-WaveDoppler radar measurements of Severe storm features. *Journal of Atmospheric and Oceanic Technology*, *16*(12), 1900–1911. https://doi.org/10.1175/1520-0426(1999)016<1900:pdpptf>2.0.co;2

Protat, A., Rauniyar, S., Delanoë, J., Fontaine, E., & Schwarzenboeck, A. (2019). W-band (95 GHz) radar attenuation in tropical stratiform ice anvils. *Journal of Atmospheric and Oceanic Technology*, *36*(8), 1463–1476. https://doi.org/10.1175/JTECH-D-18-0154.1

Rennie, M. P., Isaksen, L., Weiler, F., De Kloe, J., Kanitz, T., & Reitebuch, O. (2021). The impact of aeolus wind retrievals on ecmwf global weather forecasts. *Quarterly Journal of the Royal Meteorological Society*, *147*(740), 3555–3586. https://doi.org/10.1002/qj.4142

Rizik, A., Battaglia, A., Tridon, F., Scarsi, F., Kötsche, A., Kalesse-Los, H., et al. (2023). Impact of cross-talk on reflectivity and Doppler measurements for the wivern polarization diversity Doppler radar. *IEEE Transactions on Geoscience and Remote Sensing*, 1. https://doi.org/10.1109/TGRS.2023.3320287

Rogers, R., Reasor, P., & Lorsolo, S. (2013). Airborne Doppler observations of the inner-core structural differences between intensifying and steady-state tropical cyclones. *Monthly Weather Review*, *141*(9), 2970–2991. https://doi.org/10.1175/mwr-d-12-00357.1

Rogers, R. F., Zhang, J. A., Zawislak, J., Jiang, H., Alvey, G. R., Zipser, E. J., & Stevenson, S. N. (2016). Observations of the structure and evolution of hurricane edouard (2014) during intensity change. part ii: Kinematic structure and the distribution of deep convection. *Monthly Weather Review*, *144*(9), 3355–3376. https://doi.org/10.1175/MWR-D-16-0017.1

Sassen, K., Wang, Z., & Liu, D. (2008). The global distribution of cirrus clouds from CloudSat/CALIPSO measurements. *Geophysical Research Letters*, *113*(D00A12), D00A12. https://doi.org/10.1029/2008JD009972

Scarsi, F. E., Battaglia, A., Tridon, F., Martire, P., Dhillon, R., & Illingworth, A. (2023). Mispointing correction methods for the conically scanning wivern Doppler radar. *Atmospheric Measurement Techniques Discussions*, *2023*, 1–26. https://doi.org/10.5194/amt-2023-117

Schenkel, B. A., Edwards, R., & Coniglio, M. (2020). A climatological analysis of ambient deep-tropospheric vertical wind shear impacts upon tornadoes in tropical cyclones. *Weather and Forecasting*, *35*(5), 2033–2059. https://doi.org/10.1175/waf-d-19-0220.1

Schutgens, N. A. J. (2008). Simulated Doppler radar observations of Inhomogeneous clouds: Application to the EarthCARE space mission. *Journal of Atmospheric and Oceanic Technology*, *25*(9), 1514–1528. https://doi.org/10.1175/2007JTECHA1026.1

Scoccimarro, E., Gualdi, S., Bellucci, A., Sanna, A., Fogli, P. G., Manzini, E., et al. (2011). Effects of tropical cyclones on ocean heat transport in a high-resolution coupled general circulation model. *Journal of Climate*, *24*(16), 4368–4384. https://doi.org/10.1175/2011JCLI4104.1

Sippel, J. A., Zhang, F., Weng, Y., Tian, L., Heymsfield, G. M., & Braun, S. A. (2014). Ensemble kalman filter assimilation of hiwrap observations of hurricane karl (2010) from the unmanned global hawk aircraft. *Monthly Weather Review*, *142*(12), 4559–4580. https://doi.org/10.1175/MWR-D-14-00042.1

Stoffelen, A., Pailleux, J., Kallen, E., Vaughan, J. M., Isaksen, L., Flamant, P., et al. (2005). The atmospheric dynamics mission for global wind field measurement. *Bulletin of American Meteorological Society*, *86*(1), 73–88. https://doi.org/10.1175/bams-86-1-73

Sy, O. O., Tanelli, S., Takahashi, N., Ohno, Y., Horie, H., & Kollias, P. (2014). Simulation of EarthCARE spaceborne Doppler radar products using ground-based and airborne data: Effects of Aliasing and Nonuniform beam-filling. *IEEE Transactions of Geoscience Remote Sensing*, *52*(2), 1463–1479. https://doi.org/10.1109/TGRS.2013.2251639

Tanelli, S., Durden, S. L., Im, E., Heymsfield, G., Racette, P., & Starr, D. (2009). Next-generation spaceborne cloud profiling radars. In IEEE (Ed.). In *Radar conference* (pp. 1–4). https://doi.org/10.1109/RADAR.2009.4977116

Tanelli, S., Durden, S. L., Im, E., Pak, K. S., Reinke, D. G., Partain, P., et al. (2008). CloudSat's cloud profiling radar after two years in orbit: Performance, calibration, and processing. *IEEE Transactions of Geoscience Remote Sensing*, *46*(11), 3560–3573. https://doi.org/10.1109/TGRS.2008.2002030

Tanelli, S., Im, E., Durden, S. L., Facheris, L., & Giuli, D. (2002). The effects of Nonuniform beam filling on vertical rainfall velocity measurements with a spaceborne Doppler radar. *Journal of Atmospheric and Oceanic Technology*, *19*(7), 1019–1034. https://doi.org/10.1175/1520-0426(2002)019<1019:teonbf>2.0.co;2

Thatcher, L., & Pu, Z. (2011). How vertical wind shear affects tropical cyclone intensity change: An overview. In A. Lupo (Ed.), *Recent hurricane research (chap. 13)*. IntechOpen. https://doi.org/10.5772/15416

Tong, M., Sippel, J. A., Tallapragada, V., Liu, E., Kieu, C., Kwon, I.-H., et al. (2018). Impact of assimilating aircraft reconnaissance observations on tropical cyclone initialization and prediction using operational hwrf and gsi ensemble–variational hybrid data assimilation. *Monthly Weather Review*, *146*(12), 4155–4177. https://doi.org/10.1175/MWR-D-17-0380.1

Tourville, N., Stephens, G., DeMaria, M., & Vane, D. (2015). Remote sensing of tropical cyclones: Observations from cloudsat and a-train profilers. *Bulletin of American Meteorological Society*, *96*(4), 609–622. https://doi.org/10.1175/BAMS-D-13-00282.1

Velden, C., Lewis, W. E., Bresky, W., Stettner, D., Daniels, J., & Wanzong, S. (2017). Assimilation of high-resolution satellite-derived atmospheric motion vectors: Impact on hwrf forecasts of tropical cyclone track and intensity. *Monthly Weather Review*, *145*(3), 1107–1125. https://doi.org/10.1175/MWR-D-16-0229.1

Velden, C. S., & Bedka, K. M. (2009). Identifying the uncertainty in determining satellite-derived atmospheric motion vector height attribution. *Journal of Applied Meteorology and Climatology*, *48*(3), 450–463. https://doi.org/10.1175/2008JAMC1957.1

Wadler, J. B., Cione, J. J., Zhang, J. A., Kalina, E. A., & Kaplan, J. (2022). The effects of environmental wind shear direction on tropical cyclone boundary layer thermodynamics and intensity change from multiple observational datasets. *Monthly Weather Review*, *150*(1), 115–134. https://doi.org/10.1175/MWR-D-21-0022.1

Wadler, J. B., Rogers, R. F., & Reasor, P. D. (2018). The relationship between spatial variations in the structure of convective bursts and tropical cyclone intensification as determined by airborne Doppler radar. *Monthly Weather Review*, *146*(3), 761–780. https://doi.org/10.1175/mwr-d-17-0213.1

Walsh, K. J., McBride, J. L., Klotzbach, P. J., Balachandran, S., Camargo, S. J., Holland, G., et al. (2016). Tropical cyclones and climate change. *WIREs Climate Change*, *7*(1), 65–89. https://doi.org/10.1002/wcc.371

Wernham, D., Heliere, A., Mason, G., & Straume, A. G. (2021). Aeolus-2 mission pre-development status. In *2021 ieee international geoscience and remote sensing symposium igarss* (pp. 767–770). https://doi.org/10.1109/IGARSS47720.2021.9554716

WMO. (2023). Observing systems capability analysis and review tool. Retrieved from https://space.oscar.wmo.int/

Wu, T.-C., Liu, H., Majumdar, S. J., Velden, C. S., & Anderson, J. L. (2014). Influence of assimilating satellite-derived atmospheric motion vector observations on numerical analyses and forecasts of tropical cyclone track and intensity. *Monthly Weather Review*, *142*(1), 49–71. https://doi.org/10.1175/MWR-D-13-00023.1

Zhang, Y., Sieron, S. B., Lu, Y., Chen, X., Nystrom, R. G., Minamide, M., et al. (2021). Ensemble-based assimilation of satellite all-sky microwave radiances improves intensity and rainfall predictions for hurricane harvey (2017). *Geophysical Research Letters*, *48*(24), e2021GL096410. https://doi.org/10.1029/2021GL096410